Comput Mech (2009) 43:651–673
DOI 10.1007/s00466-008-0336-5

ORIGINAL PAPER

An extended Galerkin weak form and a point interpolation method with continuous strain field and superconvergence using triangular mesh

G. R. Liu · X. Xu · G. Y. Zhang · Y. T. Gu

Received: 19 February 2008 / Accepted: 10 September 2008 / Published online: 7 October 2008

Abstract A point interpolation method (PIM) with continuous strain field (PIM-CS) is developed for mechanics problems using triangular background mesh, in which PIM shape functions are used to construct both displacement and strain fields. The strain field constructed is continuous in the entire problem domain, which is achieved by simple linear interpolations using locally smoothed strains around the nodes and points required for the interpolation. A general parameterized functional with a real adjustable parameter α are then proposed for establishing PIM-CS models of special property. We prove theoretically that the PIM-CS has an excellent bound property: strain energy obtained using PIM-CS lies in between those of the compatible FEM and NS-PIM models of the same mesh. Techniques and procedures are then presented to compute the upper and lower bound solutions using the PIM-CS. It is discovered that an extended Galerkin (x-Galerkin) model, as special case resulted from the extended parameterized functional with $\alpha = 1$, is outstanding in terms of both performance and efficiency. Intensive numerical studies show that upper and lower bound solutions can always be obtained, there exist α values at which the solutions of PIM-CS are of superconvergence, and the x-Galerkin model is capable of producing superconvergent solutions of ultra accuracy that is about 10 times that of the FEM using the same mesh.

Keywords Finite element method · Meshfree methods · Point interpolation method · Solution bound · Superconvergence · x-Galerkin weak form

G. R. Liu
Department of Mechanical Engineering, Centre for Advanced Computations in Engineering Science (ACES),
National University of Singapore,
9 Engineering Drive 1, Singapore 117576, Singapore

G. R. Liu · X. Xu · G. Y. Zhang
Singapore-MIT Alliance (SMA), E4-04-10,
4 Engineering Drive 3, Singapore 117576, Singapore

X. Xu (✉)
College of Mathematics, Jilin University,
2699 Qianjin Street, 130012 Changchun,
People's Republic of China
e-mail: xuxu@jlu.edu.cn; smaxx@nus.edu.sg

Y. T. Gu
School of Engineering System,
Queensland University of Technology,
GPO Box 2434, Brisbane, QLD 4001, Australia

1 Introduction

To solve engineering problems, powerful numerical methods have been developed, such as the Finite Element Methods (FEM) [1–4], Finite Difference Methods [5,6], Finite Volume Methods (FVM) [7,8], and recently Meshfree Methods [9–28]. These methods and techniques not only provide solution tools for many engineering problems, but also extend our minds in the quest for even more effective and robust computational methods.

The FEM is the most widely used reliable numerical approach for engineering problems. However, there are three major shortcomings. The first is the "overly stiff" phenomenon of a fully compatible FEM model; the second concerns with the mesh distortion related problems such as the significant accuracy loss when the element mesh is heavily distorted; the third is the poor accuracy in the stress solution.

The fully compatible FEM based on the standard Galerkin weak form can usually produce a lower bound in energy norm of the exact solution to the elasticity problems (with homogenous Dirichlet boundary conditions) [1,2]. Although an FEM model based on the complementary energy principles

can produce upper bound solutions, such a model is much more difficult to establish for complicated practical engineering problems, and there exists the so-called spurious modes resulting in difficulties in solving dynamic problems [29,30]. Therefore, it is much more difficult to bound the solution from above.

In the past several decades, many efforts have been made in solving these shortcomings of fully compatible FEM models [31]. Recently, Liu et al. developed some schemes to provide some softening effects to system for solutions of high convergence and accuracy, such as the $\alpha-$FEM [32], cell-based smoothed FEM (SFEM) [33–38] , node-based smoothed FEM (NS-FEM) [39], node-based smoothed point interpolation method (NS-PIM) [40] and edged-based smoothed FEM (ES-FEM) [41]. Nguyen et al. investigated further the properties of SFEM and extended applications [42–44]. These methods introduce the strain smoothing operations [45] and point interpolation method into FEM procedures, and worked very effectively for various problems in science and engineering [46–51]. Liu [29] have recently presented a theoretical framework for those methods, where G spaces are established for accommodating discontinuous functions and hence different techniques for function approximation (such as PIM [40] and RPIM [48]) with various ways for smoothing operations. This new theory based on G spaces provides a new foundation for developing a wide class of new efficient computational methods, such as the meshfree methods of smoothed PIM family and the smoothed FEM family.

When the node-based strain smoothing operations are used, the NS-PIM provides an upper bound solution of the exact solution in energy norm for general elasticity problems (with homogenous essential boundary conditions). The detailed discussions and theoretical analysis on the bound properties and convergence for NS-PIM can be found in Refs. [30,49]. It has been shown that the node-based smoothing operation can produces a model that is sufficiently "softer" than the real solids, and hence can offer an upper bound to the exact solutions. The important point is that the fully compatible FEM and the node-based smoothed PIM play complementary roles in the numerical solution bounds, and hence we have now a general way to bound the solution from the both sides of the exact solution using a usual FEM mesh. This technique has also been extended to establish real-time computational model with bounds for inverse problems [52,53].

Note that the strain field in an NS-PIM is constant in each smoothing domain, and hence is a zero order approximation of the compatible strain field. To provide a better approximation for the strain field, this work constructs a continuous piecewisely linear strain field using the PIM shape functions and the strain smoothing technique. The PIM-CS is equipped with a real adjustable parameter α for solutions of superconvergence. It is proven that the PIM-CS can produce either a "softer" or a "stiffer" stiffness matrix than that of real model, and hence provide an upper or lower bound to the exact solution in the energy norm, as desired. It is also possible for PIM-CS to produce a solution that is almost the "exact" solution using a finite number of triangular cells. It is discovered that an extended Galerkin (x-Galerkin) model, as special case resulted from the extended parameterized functional with $\alpha = 1$, is outstanding in terms of both performance and efficiency. It is capable of producing superconvergent solutions of ultra accuracy that is about 10 times that of the FEM using the same mesh.

The paper is outlined as follows. Section 2 briefs the linear elasticity, and Sect. 3 gives a briefing on NS-PIM. The idea of the PIM-CS is presented in Sect. 4. The convergence and bound properties of the PIM-CS are presented and theoretically proven in Sect. 5. In Sect. 6, the unique superconvergent properties of the PIM-CS are discussed. In Sect. 7, numerical examples are presented and discussed to verify the theorems and properties of the PIM-CS. Conclusions are drawn in Sect. 8.

2 Brief on basic equations of linearity elasticity

Consider a 2D static elasticity problem governed by the equilibrium equation in the domain Ω bounded by $\Gamma(\Gamma = \Gamma_u + \Gamma_t,\ \Gamma_u \cap \Gamma_t = 0)$ as

$$\mathbf{L}_{\mathrm{d}}^{\mathrm{T}}\boldsymbol{\sigma} + \mathbf{b} = 0 \text{ in } \Omega \tag{1}$$

where $\mathbf{L}_{\mathrm{d}}$ is a matrix of differential operators defined as

$$\mathbf{L}_{\mathrm{d}} = \begin{bmatrix} \frac{\partial}{\partial x_1} & 0 & \frac{\partial}{\partial x_2} \\ 0 & \frac{\partial}{\partial x_2} & \frac{\partial}{\partial x_1} \end{bmatrix}^{\mathrm{T}} \tag{2}$$

$\boldsymbol{\sigma}^{\mathrm{T}} = (\sigma_{11}, \sigma_{22}, \sigma_{12})$ is the vector of stresses, $\mathbf{b}^{\mathbf{T}} = (b_1, b_2)$ is the vector of body forces. The stresses relate the strains via the generalized Hook's law:

$$\boldsymbol{\sigma} = \mathbf{D}\boldsymbol{\varepsilon} \tag{3}$$

where $\mathbf{D}$ is the matrix of material constants [54], and $\boldsymbol{\varepsilon}^{\mathrm{T}} = (\varepsilon_{11}, \varepsilon_{22}, \gamma_{12})$ (with $\gamma_{12} = 2\varepsilon_{12}$) is the vector of strains given by

$$\boldsymbol{\varepsilon} = \mathbf{L}_{\mathrm{d}}\mathbf{u} \tag{4}$$

Essential boundary conditions are:

$$\mathbf{u} = \mathbf{u}_0 \text{ on } \Gamma_{\mathbf{u}} \tag{5}$$

where $\mathbf{u}^{\mathbf{T}} = (u_1, u_2)$ is the vector of the displacement and $\mathbf{u}_0$ is the vector of the prescribed displacements on the essential boundary $\Gamma_{\mathbf{u}}$. In this paper, we consider only homogenous essential boundary conditions $\mathbf{u}_0 = \mathbf{0}$.

Natural boundary conditions are:

$$\mathbf{L}_{\mathrm{n}}^{\mathrm{T}}\boldsymbol{\sigma} = \mathbf{T} \text{ on } \Gamma_{\mathbf{t}} \tag{6}$$

where $\mathbf{T}$ is the vector of the prescribed tractions on the natural boundary Γ_{t}, and $\mathbf{L}_{\mathrm{n}}$ is the matrix of unit outward normal which can be expressed as

$$\mathbf{L}_{\mathrm{n}} = \begin{bmatrix} n_{x_1} & 0 & n_{x_2} \\ 0 & n_{x_2} & n_{x_1} \end{bmatrix}^{\mathrm{T}} \tag{7}$$

3 Briefing on the NS-PIM (or LC-PIM) [40]

In the node-based smoothed PIM (NS-PIM), the problem domain is first discretized by a set of background triangular cells as shown in Fig. 1. The total number of nodes, cells, and edges in the problem domain are denoted as N_n, N_c and N_e, respectively. The displacements in a cell are approximated using PIM shape functions:

$$\overline{\mathbf{u}}(\mathbf{x}) = \sum_{i \in n_e} \boldsymbol{\Phi}_i(\mathbf{x})\overline{\mathbf{d}}_i \tag{8}$$

where n_e is the set of nodes of the local support domain containing $\mathbf{x}$ which is in general beyond the cell, $\overline{\mathbf{d}}_i$ is a vector of displacements at this set of nodes, and

$$\boldsymbol{\Phi}_i(\mathbf{x}) = \begin{bmatrix} \varphi_i(\mathbf{x}) & 0 \\ 0 & \varphi_i(\mathbf{x}) \end{bmatrix} \tag{9}$$

is the matrix of the shape function for node i which is constructed generally using the PIM procedure and hence is of Delta function property.

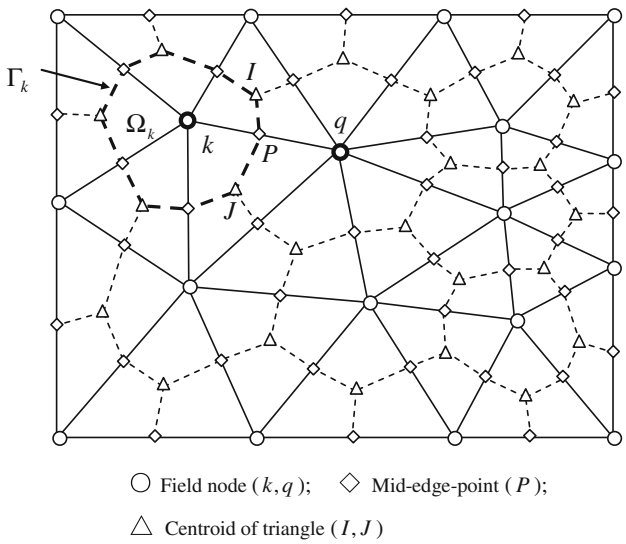

Fig. 1 Triangular elements and the smoothing cells created by sequentially connecting the centroids with the mid-edge-points of the surrounding triangles of a node

In carrying out the numerical integration with proper smoothing operations, the problem domain Ω is divided into smoothing domains Ω_k containing node k, as shown in Fig. 1. The smoothing domain Ω_k is constructed using a triangular element mesh by connecting sequentially the mid-edge-point P to the centroids I of the triangles. The boundary of Ω_k is labeled as Γ_k and the union of all Ω_k forms Ω exactly.

NS-PIM uses constant strain for each of the smoothing domain defined by [45]

$$\overline{\boldsymbol{\varepsilon}}_k \equiv \overline{\boldsymbol{\varepsilon}}(\mathbf{x}_k) = \frac{1}{A_k}\int_{\Omega_k} \tilde{\boldsymbol{\varepsilon}}(\mathbf{x})\mathrm{d}\Omega \tag{10}$$

where $A_k = \int_{\Omega_k} \mathrm{d}\Omega$ is the area of smoothing domain for node k, and $\tilde{\boldsymbol{\varepsilon}}(\mathbf{x}) = \mathbf{L}_{\mathrm{d}}\overline{\mathbf{u}}$ is the compatible strain.

As the NS-PIM is variationally consistent when the solution is sought from a Hilbert space [29] and the convergence is ensured when the solution is in a G space [55]. The assumed displacement $\overline{\mathbf{u}}$ and the corresponding assumed strains $\overline{\boldsymbol{\varepsilon}}$ satisfies the generalized smoothed Galerkin weak form [29]

$$\int_{\Omega} \delta\overline{\boldsymbol{\varepsilon}}^{\mathrm{T}}(\overline{\mathbf{u}})\mathbf{D}\overline{\boldsymbol{\varepsilon}}(\overline{\mathbf{u}})\mathrm{d}\Omega - \int_{\Omega} \delta\overline{\mathbf{u}}^{\mathrm{T}}\mathbf{b}\mathrm{d}\Omega - \int_{\Gamma_t} \delta\overline{\mathbf{u}}^{\mathrm{T}}\mathbf{T}\mathrm{d}\Gamma = 0 \tag{11}$$

Substituting Eqs. (8) and (10) into Eq. (11) yields the discretized system equation:

$$\overline{\mathbf{K}}\,\overline{\mathbf{d}} = \overline{\mathbf{f}}, \tag{12}$$

where

$$\overline{\mathbf{K}} = \sum_{k=1}^{N} \overline{\mathbf{K}}_{ij}^{(k)} = \sum_{k=1}^{N} \int_{\Omega_k} \overline{\mathbf{B}}_i^{\mathrm{T}}(\mathbf{x}_k)\mathbf{D}\overline{\mathbf{B}}_j^{\mathrm{T}}(\mathbf{x}_k)\mathrm{d}\Omega \tag{13}$$

$$\overline{\mathbf{f}}_i = \int_{\Gamma_t} \Phi_i \mathbf{T}\mathrm{d}\Gamma + \int_{\Omega} \Phi_i \mathbf{b}\mathrm{d}\Omega \tag{14}$$

4 The idea of the PIM-CS

4.1 Choice of the shape functions

In the PIM-CS, the point interpolation method (PIM) is used to construct shape functions using a small set of nodes distributed in a local support domain. As the triangular cells can be generated automatically [17], background cells of triangles are employed in the present PIM-CS to select nodes for both shape function and strain field constructions. The details on the construction and detailed distribution of the PIM shape function can be found in Refs. [17,40]. Using

PIM shape functions, the displacement field in the PIM-CS can be approximated as follows.

$$\hat{\mathbf{u}}(\mathbf{x}) = \sum_{i \in n_e} \mathbf{\Phi}_i(\mathbf{x}) \hat{\mathbf{d}}_i \tag{15}$$

where n_e is the set of nodes in the support domain containing $\mathbf{x}$, $\hat{\mathbf{d}}_i$ is the vector of nodal displacements and

$$\mathbf{\Phi}_i(\mathbf{x}) = \begin{bmatrix} \varphi_i(\mathbf{x}) & 0 \\ 0 & \varphi_i(\mathbf{x}) \end{bmatrix} \tag{16}$$

is the matrix of the PIM shape functions for node i.

The procedure for the shape function construction of PIM-CS is simple and possesses the following features: (1) it uses local supporting nodes selected based on triangular cells, which overcomes the singular moment matrix issue, guarantees the linearly independence of these shape functions, and ensures the efficiency in computing PIM shape function; (2) shape functions generated using polynomial basis functions with at least linear terms ensure that the PIM shape functions possess at least linearly consistency; (3) the shape functions are of the Delta function property, which facilitates easy implementation of essential boundary conditions; and (4) the shape functions are linearly independent and form a basis for field function construction.

4.2 Construction for continuous strain field

In the present PIM-CS, a Ω_k shown in Fig. 1 is further divided into M sub-domains $\Omega_{k,1}, \Omega_{k,2}, \ldots, \Omega_{k,M}$. This is done by connecting node k to the centroids of the surrounding triangles, as shown in Fig. 2.

The PIM-CS assumes that strain $\hat{\boldsymbol{\varepsilon}}$ at any points within a sub-triangular domain $\Omega_{k,i}$ ($k = 1, \ldots, N$, $i = 1, \ldots, M$) are obtained by simple linear point interpolation:

$$\hat{\boldsymbol{\varepsilon}}(\mathbf{x}) = L_1(\mathbf{x})\boldsymbol{\varepsilon}_k + L_2(\mathbf{x})\boldsymbol{\varepsilon}_P + L_3(\mathbf{x})\boldsymbol{\varepsilon}_I \tag{17}$$

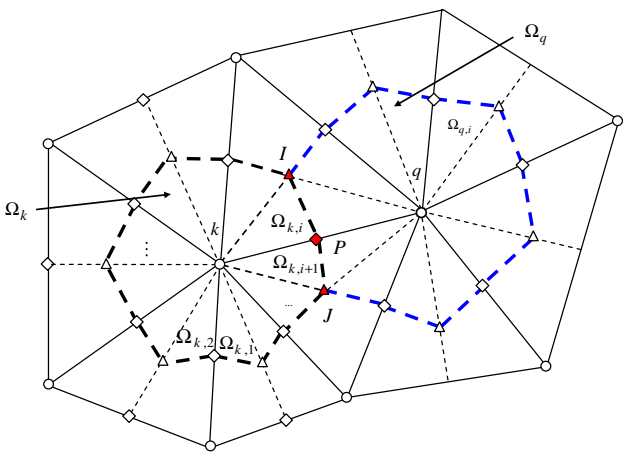

Fig. 2 Illustration of triangular sub-domains $\Omega_{k,i}$ within domain Ω_k that is adjacent to Ω_q

where L_1, L_2, L_3 is the area coordinates for $\Omega_{k,i}$; $\boldsymbol{\varepsilon}_k$, $\boldsymbol{\varepsilon}_P$, $\boldsymbol{\varepsilon}_I$ are the strains at the vertices of sub-triangular $\Omega_{k,i}$: node k, midpoint P of a cell-edge and centriod I of $\Omega_{k,i}$. These strains are then assumed to be the averaged strains in the smoothing domains containing the vertices using the strain smoothing operation [45].

$$\bar{\boldsymbol{\varepsilon}} \equiv \frac{1}{A} \int_{\Omega_A} \tilde{\boldsymbol{\varepsilon}}(\mathbf{x}) \mathrm{d}\xi \tag{18}$$

where $\tilde{\boldsymbol{\varepsilon}}(\mathbf{x}) = \mathbf{L_d}\hat{\mathbf{u}}(\mathbf{x})$ is the compatible strain, Ω_A represents the smoothing domain of a interested point, A is the area of smoothing domain Ω_A.

The smoothing domain Ω_A is usually a localized subdomain in the vicinity of the interested point $\mathbf{x}$, and changes with point $\mathbf{x}$. Hence, it can be different from that of other points and can be generally overlapping. The issue now is how to form the smoothing domain for a given point. In this work, we follow the compact principle suggested in the gradient smoothing method (GSM [56,57]): the smoothing domain of a point should be as compact as possible containing the point. Based on the locations of these points k, I and P, we form three types of smoothing domains as shown in Fig. 3. The first type of smoothing domain Ω_k is the node-associated gradient smoothing domain (nGSD) for the approximation of strain $\boldsymbol{\varepsilon}_k$ at node k. It is formed by connecting sequentially centroids of triangles with midpoints of relevant cell-edges. The second type of smoothing domain Ω_I is formed by a background triangular cell for approximating $\boldsymbol{\varepsilon}_I$ at the centroid of the cell. It is called centroid-associated gradient smoothed domain (cGSD). The third type of smoothing domain Ω_P is named midpoint-associated gradient smoothed domain (mGSD) used for the evaluation of the strain $\boldsymbol{\varepsilon}_P$ at the midpoint of a cell-edge. The mGSD is formed by connecting the end-nodes of the cell-edge with the centroids of the triangles on the both sides of the cell-edge.

4.3 Strain construction schemes

Using Eq. (18), the strains $\boldsymbol{\varepsilon}_k$, $\boldsymbol{\varepsilon}_P$, $\boldsymbol{\varepsilon}_I$ can now be evaluated as the averaged strains in smoothing domains Ω_k, Ω_P, Ω_I, respectively.

(1) The strain $\boldsymbol{\varepsilon}_I$ at centriod of a triangular cell is given by

$$\boldsymbol{\varepsilon}_I = \widehat{\boldsymbol{\varepsilon}}_I \equiv \frac{1}{A_I} \int_{\Omega_I} \mathbf{L_d}\hat{\mathbf{u}}(\mathbf{x})\, \mathrm{d}\Omega, \tag{19}$$

(2) The strain $\boldsymbol{\varepsilon}_P$ is the smoothed strain over the edge-based smoothed domain Ω_P

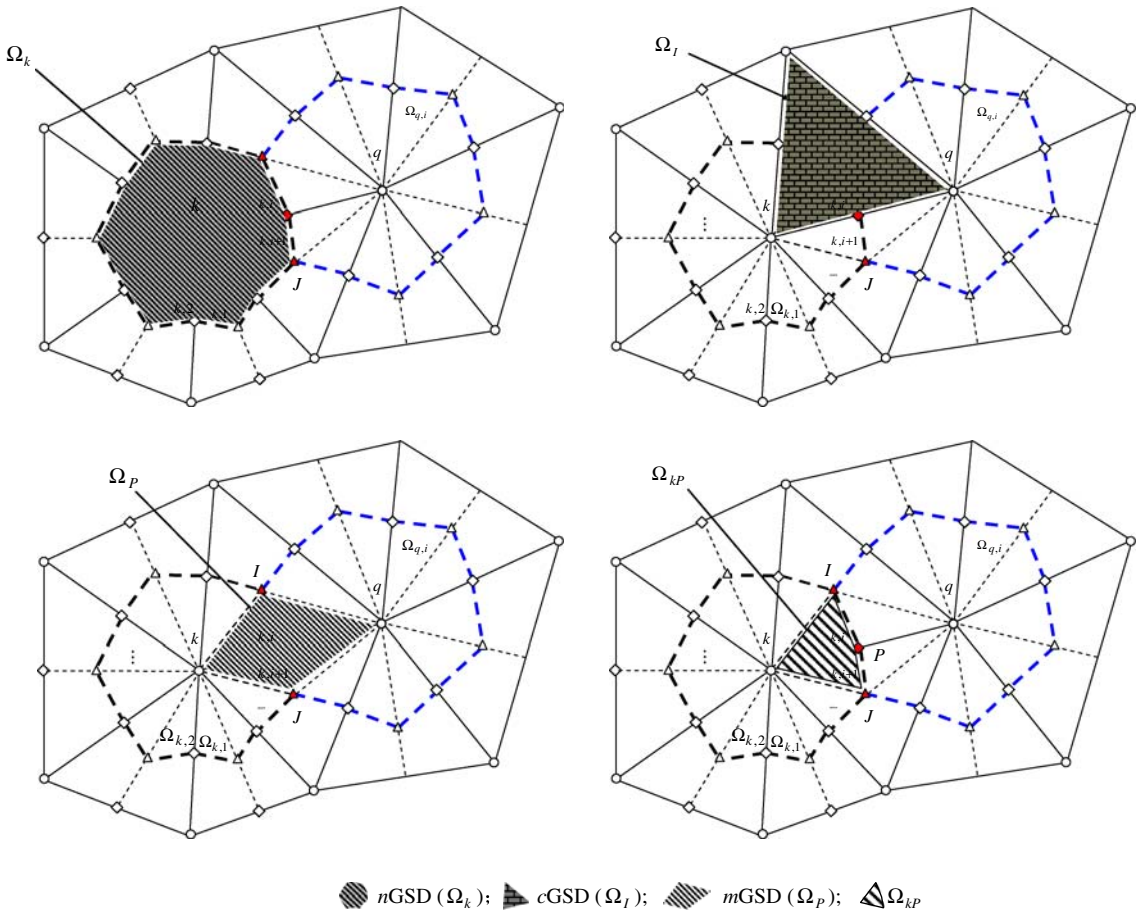

Fig. 3 Illustration of types of smoothing domains for the evaluation of the strains at points k, I and P

$$\boldsymbol{\varepsilon}_P = \breve{\boldsymbol{\varepsilon}}_P \equiv \frac{1}{A_P}\int_{\Omega_P} \mathbf{L_d}\hat{\mathbf{u}}(\mathbf{x})\,\mathrm{d}\Omega, \tag{20}$$

(3) The strain $\boldsymbol{\varepsilon}_k$ at a node is the smoothed strain in smoothing domain Ω_k

$$\boldsymbol{\varepsilon}_k = \bar{\boldsymbol{\varepsilon}}_k \equiv \frac{1}{A_k}\int_{\Omega_k} \mathbf{L_d}\hat{\mathbf{u}}(\mathbf{x})\,\mathrm{d}\Omega, \tag{21}$$

where A_I, A_P and$A_k$are the areas of the domain Ω_I, Ω_P and Ω_k, respectively.

The strain obtained using Eqs. (17), (19)–(21) is therefore continuous in the entire problem domain Ω. To explain this, consider two adjacent node domains Ω_k and Ω_q as shown in Fig. 2. The interface edges of these two domains are the edge $I-P-J$. As the linear interpolation Eq. (17) is used for strain evaluation, Eqs. (19) and (20) show that the strains at edge $I-P-J$ for domain Ω_k are the same as that for domain Ω_q. The similar situation occurs for the strains at edges $k-I$ and $k-P$. Therefore, the strain field is continuous in the entire problem domain Ω.

The overall procedure of strain field construction in the PIM-CS is as follows. The displacement at any point in a triangular cell is first approximated via point interpolation using Eq. (15). The strains at points k, I and $P$are then evaluated using Eqs. (19)–(21). The strain field is next constructed using again point interpolation using Eq. (17). Therefore, the strain depends entirely on the assumed displacement field, no additional degrees of freedoms are introduced, and the dimension of the discretized system equation in our PIM-CS model will be exactly the same as the FEM model of the same mesh.

Note that in the NS-PIM, the assumed strain is constant in each node-based smoothed domain Ω_k, it thus takes into account of only the averaged strain in the smoothing domain of node k. The difference in strain gradient in the individual triangular sub-domains $\Omega_{k,i}$ is ignored. In the FEM, on the other hand, the strain in each individual sub-domain is obtained using $\tilde{\boldsymbol{\varepsilon}} = \mathbf{L_d}\tilde{\mathbf{u}}$, which counts fully the compatible strain field in $\Omega_{k,i}$ but does not consider the overall strain variations in Ω_k. The PIM-CS considers not only the averaged

feature in strain field over Ω_k, but also the local effects of $\Omega_{k,i}$. Hence, it is expected to have excellent properties.

We state now the following theorem for later use.

Theorem 1 (Equivalence for norms of assumed and compatible strain fields) *In the PIM-CS settings detailed in Sect. 4.3, there exists a non-zero positive constant c_{ac} such that*

$$\left\|\hat{\boldsymbol{\varepsilon}}(\mathbf{w})\right\|_0 \leq c_{ac}\,\|\tilde{\boldsymbol{\varepsilon}}(\mathbf{w})\|_0\,, \tag{22}$$

and equivalently there exists a non-zero positive constant c_{ca} such that

$$\|\tilde{\boldsymbol{\varepsilon}}(\mathbf{w})\|_0 \leq c_{ca}\left\|\hat{\boldsymbol{\varepsilon}}(\mathbf{w})\right\|_0. \tag{23}$$

which means that the norm $\left\|\hat{\boldsymbol{\varepsilon}}(\mathbf{w})\right\|_0$ is equivalent to norm $\|\tilde{\boldsymbol{\varepsilon}}(\mathbf{w})\|_0$.

Proof For simplicity in expressions, we first denote the strains at vertices of the sub-domain $\Omega_{k,\,i}$ as:

$$\hat{\boldsymbol{\varepsilon}}_1 = \bar{\boldsymbol{\varepsilon}}_k, \quad \hat{\boldsymbol{\varepsilon}}_2 = \breve{\boldsymbol{\varepsilon}}_P, \quad \hat{\boldsymbol{\varepsilon}}_3 = \widehat{\boldsymbol{\varepsilon}}_I \tag{24}$$

Using Eq. (17), the strain in each of sub-domains $\Omega_{k,i}$ can now be written in a more concise form of

$$\hat{\boldsymbol{\varepsilon}}(\mathbf{x}) = \sum_{\gamma=1}^{3} L_\gamma(\mathbf{x})\hat{\boldsymbol{\varepsilon}}_\gamma. \tag{25}$$

From Eq. (17) and Eq. (36), we have

$$\begin{aligned}
\left\|\hat{\boldsymbol{\varepsilon}}(\mathbf{w})\right\|_0^2 &= \sum_{k=1}^{N}\sum_{i=1}^{M}\int_{\Omega_{k,\,i}}\sum_{\beta=1}^{3}[L_\beta\hat{\boldsymbol{\varepsilon}}_\beta^{\mathrm{T}}(\mathbf{w})]\sum_{\gamma=1}^{3}[L_\gamma\hat{\boldsymbol{\varepsilon}}_\gamma(\mathbf{w})]\,\mathrm{d}\Omega \\
&= \sum_{k=1}^{N}\sum_{i=1}^{M}\sum_{\beta,\,\gamma=1}^{3}\left[\hat{\boldsymbol{\varepsilon}}_\beta^{\mathrm{T}}(\mathbf{w})\;\hat{\boldsymbol{\varepsilon}}_\gamma(\mathbf{w})\;\underbrace{\int_{\Omega_{k,\,i}} L_\beta L_\gamma\,\mathrm{d}\Omega}_{\eta_{\beta\gamma}}\right] \\
&= \sum_{k=1}^{N}\sum_{i=1}^{M}\sum_{\beta,\,\gamma=1}^{3}[\eta_{\beta\gamma}\;\hat{\boldsymbol{\varepsilon}}_\beta^{\mathrm{T}}(\mathbf{w})\;\hat{\boldsymbol{\varepsilon}}_\gamma(\mathbf{w})]
\end{aligned} \tag{26}$$

where $\eta_{\beta\gamma} = \int_{\Omega_{k,\,i}} L_\beta L_\gamma\,\mathrm{d}\Omega > 0$. Substituting Eq. (18) into (26) yields

$$\left\|\hat{\boldsymbol{\varepsilon}}(\mathbf{w})\right\|_0^2 = \left|\sum_{k=1}^{N}\sum_{i=1}^{M}\sum_{\beta,\gamma=1}^{3}\eta_{\beta\gamma}\left[\frac{1}{A_\gamma}\frac{1}{A_\beta}\int_{\Omega_\gamma}\tilde{\boldsymbol{\varepsilon}}^{\mathrm{T}}(\mathbf{w})\mathrm{d}\xi\int_{\Omega_\beta}\tilde{\boldsymbol{\varepsilon}}(\mathbf{w})\mathrm{d}\xi\right]\right|. \tag{27}$$

Applying for the triangular and Cauchy-Schwartz inequalities, we have

$$\begin{aligned}
\left\|\hat{\boldsymbol{\varepsilon}}(\mathbf{w})\right\|_0^2 &\leq \sum_{k=1}^{N}\sum_{i=1}^{M}\sum_{\beta,\gamma=1}^{3}\eta_{\beta\gamma} \\
&\quad\times\left[\frac{1}{A_\gamma}\frac{1}{A_\beta}\int_{\Omega_\gamma}\|\tilde{\boldsymbol{\varepsilon}}(\mathbf{w})\|_0\mathrm{d}\xi\cdot\int_{\Omega_\beta}\|\tilde{\boldsymbol{\varepsilon}}(\mathbf{w})\|_0\,\mathrm{d}\xi\right] \\
&\leq \sum_{k=1}^{N}\sum_{i=1}^{M}\sum_{\beta,\gamma=1}^{3}\eta_{\beta\gamma}\left[\|\tilde{\boldsymbol{\varepsilon}}(\mathbf{w})\|_0\,\|\tilde{\boldsymbol{\varepsilon}}(\mathbf{w})\|_0\right] \\
&\leq \eta^{\max}\sum_{k=1}^{N}\sum_{i=1}^{M}\left[\|\tilde{\boldsymbol{\varepsilon}}(\mathbf{w})\|_0\,\|\tilde{\boldsymbol{\varepsilon}}(\mathbf{w})\|_0\right] \\
&= \eta^{\max}\,\|\tilde{\boldsymbol{\varepsilon}}(\mathbf{w})\|_0^2
\end{aligned} \tag{28}$$

where $\eta^{\max} = \max_{k,\,i}(\eta_{\beta\gamma})$. Letting $c_{ac} = \sqrt{\eta^{\max}}$ we hence have Eq. (22).

On the other hand, if $\left\|\hat{\boldsymbol{\varepsilon}}(\mathbf{w})\right\|_0 = 0$, then $\hat{\boldsymbol{\varepsilon}}(\mathbf{w})$ must be zero in all the sub-domain $\Omega_{k,\,i}$, which indicates that all the $\boldsymbol{\varepsilon}_k$, $\boldsymbol{\varepsilon}_P$, $\boldsymbol{\varepsilon}_I$ in all $\Omega_{k,\,i}$ have to be zero, because of the linearly independence of L_1, L_2, and L_3 for each $\Omega_{k,\,i}$. Therefore, the total strain sampling points in the problem domain become $N_s = N_c + N_e + N_n$, and the independent number of (energy) equations becomes $3N_s$ (one equation per strain component), that is far larger than total number of nodal degree of freedoms (DOFs) for any possible meshing of the domain, that is $2N_n$ (two displacement DOFs per node). Due to the independence of the strain matrix obtained from the linearly independent PIM shape functions, the only possibility for all these $\boldsymbol{\varepsilon}_k$, $\boldsymbol{\varepsilon}_P$, $\boldsymbol{\varepsilon}_I$ being zero in the entire problem domain is that all the nodal displacements must be zero [29], and thus the compatible strain $\tilde{\boldsymbol{\varepsilon}}$ must be zero everywhere, which result in $\|\tilde{\boldsymbol{\varepsilon}}(\mathbf{w})\|_0 = 0$. This means that $\left\|\hat{\boldsymbol{\varepsilon}}(\mathbf{w})\right\|_0 = 0$ will surely lead to $\|\tilde{\boldsymbol{\varepsilon}}(\mathbf{w})\|_0 = 0$. Furthermore, if $\left\|\hat{\boldsymbol{\varepsilon}}(\mathbf{w})\right\|_0 > 0$, then $\hat{\boldsymbol{\varepsilon}}(\mathbf{w})$ will be non-zero in at least one sub-domain $\Omega_{k,\,i}$. Using Eq. (18), we know that any non-zero smoothed strain implies an existence of non-zero compatible strains in at least one of the triangular cells connected to $\Omega_{k,\,i}$, which results in $\|\tilde{\boldsymbol{\varepsilon}}(\mathbf{w})\|_0 > 0$. Therefore, there always exists a non-zero positive content c_{ca} such that Eq. (23) holds. This completes the proof of Theorem 1. □

5 Variational principle for PIM-CS

Displacement-based FEM models are formulated based on the standard Galerkin weak form that demands the assumed displacement field with full compatibility. The element behaves generally overly stiff, especially when a triangular mesh is used. To formulating PIM-CS, we need first to

construct a general parameterized mixed functional for our variational formulation.

5.1 A general parameterized mixed energy functional

A general parameterized mixed energy functional is defined as

$$\hat{\Pi}(\mathbf{v}) = \int_{\Omega} [\alpha U_{EG} + (1-\alpha)U_{HR} - \mathbf{v}^{\mathrm{T}}\mathbf{b}]\mathrm{d}\Omega - \int_{\Gamma_t} \mathbf{v}^{\mathbf{T}}\mathbf{T}\mathrm{d}\Gamma, \tag{29}$$

where the following two energy functionals are mixed together.

$$U_{EG} = \frac{1}{2}\hat{\boldsymbol{\varepsilon}}^{\mathrm{T}}(\mathbf{v})\mathbf{D}\hat{\boldsymbol{\varepsilon}}(\mathbf{v}), \tag{30}$$

$$U_{HR} = -\frac{1}{2}\hat{\boldsymbol{\varepsilon}}^{\mathrm{T}}(\mathbf{v})\mathbf{D}\hat{\boldsymbol{\varepsilon}}(\mathbf{v}) + \hat{\boldsymbol{\varepsilon}}^{\mathrm{T}}(\mathbf{v})\mathbf{D}\tilde{\boldsymbol{\varepsilon}}(\mathbf{v}), \tag{31}$$

and α is an adjustable parameter that controls the mixture and is generalized here to a finite real number: $\alpha \in (-\infty, +\infty)$. This generalization gives us much needed more rooms for exploring possible PIM-CS models of excellent properties.

Substituting Eqs. (17), (19)–(21) into (29), and invoking the stationary condition of Eq. (29), lead to the discretized system equations in the following matrix form.

$$\hat{\mathbf{K}}\hat{\mathbf{d}} = \hat{\mathbf{f}}, \tag{32}$$

where

$$\hat{\mathbf{f}} = -\int_{\Omega} \boldsymbol{\Phi}^{\mathrm{T}}\mathbf{b}\mathrm{d}\Omega + \int_{\Gamma_t} \boldsymbol{\Phi}^{\mathrm{T}}\mathbf{T}\mathrm{d}\Gamma \tag{33}$$

and $\hat{\mathbf{K}}$ is the stiffness matrix and will be given in details later.

5.2 Special PIM-CS schemes: x-Galerkin formulation

We can now obtain different schemes by adjusting α:

Scheme 1: when $\alpha = 0$, Eq. (29) is the energy functional used in the standard Hellinger- Reissner variational principle [58].

Scheme 2: when $\alpha = 1$, Eq. (29) becomes the following new energy functional

$$\Pi_{Ext}(\mathbf{v}) = \int_{\Omega} \frac{1}{2}\hat{\boldsymbol{\varepsilon}}^{\mathbf{T}}(\mathbf{v})\mathbf{D}\hat{\boldsymbol{\varepsilon}}(\mathbf{v})\Omega - \int_{\Omega} \mathbf{v}^{\mathrm{T}}\mathbf{b}\mathrm{d}\Omega - \int_{\Gamma_t} \mathbf{v}^{\mathrm{T}}\mathbf{T}\mathrm{d}\Gamma, \tag{34}$$

which is termed as the extended Galerkin (x-Galerkin) functional in this paper. We will see later some superior properties of the x-Galerkin model built using this functional. For now, we need to examine the viability of the x-Galerkin formulation.

Note that the orthogonal condition

$$\int_{\Omega} \hat{\boldsymbol{\varepsilon}}^{\mathbf{T}}(\mathbf{v})\mathbf{D}\hat{\boldsymbol{\varepsilon}}(\mathbf{v})\mathrm{d}\Omega = \int_{\Omega} \hat{\boldsymbol{\varepsilon}}^{\mathbf{T}}(\mathbf{v})\mathbf{D}\tilde{\boldsymbol{\varepsilon}}(\mathbf{v})\mathrm{d}\Omega \tag{35}$$

is not generally satisfied by the assumed strain fields in the present PIM-CS. When the x-Galerkin functional is used, this model is *not* in general variationally consistent. This is the major difference between the x-Galerkin weak form and the so-called generalized smoothed Galerkin weak form given in Eq. (11). The latter is always variationally consistent if the solution is sought in a Hilbert space as proven by Liu et al. [30]. Therefore, we have to prove the convergence for our new x-Galerkin model. Note that the proofs given in this paper is only for functions in H spaces, as the proofs for functions in G spaces are much more involved and need much more detailed analysis, as shown in [55].

5.3 Convergence proof of the x-Galerkin formulation

Let $\mathbf{w} = (w_1, w_2)^{\mathrm{T}}$ and $\mathbf{v} = (v_1, v_2)^{\mathrm{T}}$ be vector functions of two component functions. The inner product and the associate norm of vectors is defined as

$$(\mathbf{w},\ \mathbf{v})_0 = \int_{\Omega} \mathbf{w}^{\mathrm{T}}\mathbf{v}\ \mathrm{d}\Omega, \quad \|\mathbf{v}\|_0 = [(\mathbf{v}, \mathbf{v})_0]^{1/2} \tag{36}$$

and

$$(\mathbf{w}, \mathbf{v})_1 = (\nabla\mathbf{w}, \nabla\mathbf{v})_0 + (\mathbf{w}, \mathbf{v})_0, \quad \|\mathbf{v}\|_1 = [(\mathbf{v}, \mathbf{v})_1]^{1/2} \tag{37}$$

where

$$\nabla\mathbf{v} = \begin{bmatrix} \partial v_1/\partial x_1 & \partial v_1/\partial x_2 \\ \partial v_2/\partial x_1 & \partial v_2/\partial x_2 \end{bmatrix}, \tag{38}$$

and

$$(\nabla\mathbf{w},\ \nabla\mathbf{v})_0 = \sum_{i=1}^{2}\sum_{j=1}^{2}\left[\frac{\partial w_i}{\partial x_j}\frac{\partial v_i}{\partial x_j}\right]. \tag{39}$$

Therefore, the weak formulation of Eq. (1) through (6) is to find a $\mathbf{w} \in \mathrm{V}_h \subset \mathrm{V}$ where $\mathrm{V} = \left\{\mathbf{v} \in H^1(\Omega)\text{: } \mathbf{v}|_{\Gamma_{\mathbf{u}}} = \mathbf{0}\right\}$ and $H^1(\Omega)$ is a Hilbert space, such that

$$a(\mathbf{w}, \mathbf{v}) = (\mathbf{b}, \mathbf{v})_0 + \int_{\Gamma_t} \mathbf{v}^{\mathrm{T}}\mathbf{T}\ \mathrm{d}\Gamma, \quad \forall\mathbf{v} \in \mathrm{V}_h, \tag{40}$$

where V_h is a subspace of finite dimension in a Hilbert space. The bilinear form a is defined as

$$a(\mathbf{w}, \mathbf{v}) = \int_{\Omega} \hat{\boldsymbol{\varepsilon}}^{\mathrm{T}}(\mathbf{w})\ \mathbf{D}\ \hat{\boldsymbol{\varepsilon}}(\mathbf{v})\ \mathrm{d}\Omega \tag{41}$$

in which $\hat{\boldsymbol{\varepsilon}}$ is defined by Eq. (17).

Theorem 2 (existence and uniqueness Theorem) *Let Ω be a domain with piecewise smoothing boundary, and suppose $\Gamma_{\mathbf{u}}$ has positive two-dimensional measure. Then the variational problem (40) of linear elasticity for stable solids has exactly one solution.*

Proof It is seen that the bilinear form (41) is symmetric for the symmetry of the elastic constants. From Eq. (41) we have

$$\begin{aligned} a(\mathbf{w},\mathbf{w}) &= \int_{\Omega} \hat{\boldsymbol{\varepsilon}}^{\mathrm{T}}(\mathbf{w})\, \mathbf{D}\hat{\boldsymbol{\varepsilon}}(\mathbf{w})\, \mathrm{d}\Omega \\ &= \int_{\Omega} \hat{\boldsymbol{\varepsilon}}^{\mathrm{T}}(\mathbf{w})\, \underbrace{\mathbf{U}^{\mathrm{T}}\boldsymbol{\Lambda}\mathbf{U}}_{\mathbf{D}}\, \hat{\boldsymbol{\varepsilon}}(\mathbf{w})\, \mathrm{d}\Omega \\ &= \int_{\Omega} [\mathbf{U}\hat{\boldsymbol{\varepsilon}}(\mathbf{w})]^{\mathrm{T}}\boldsymbol{\Lambda}[\mathbf{U}\hat{\boldsymbol{\varepsilon}}(\mathbf{w})]\, \mathrm{d}\Omega \\ &\le \lambda_{\max} \int_{\Omega} [\mathbf{U}\hat{\boldsymbol{\varepsilon}}(\mathbf{w})]^{\mathrm{T}}[\mathbf{U}\hat{\boldsymbol{\varepsilon}}(\mathbf{w})]\, \mathrm{d}\Omega \\ &= \lambda_{\max} \int_{\Omega} \hat{\boldsymbol{\varepsilon}}^{\mathrm{T}}(\mathbf{w})\, \mathbf{U}^{\mathrm{T}}\mathbf{U}\, \boldsymbol{\varepsilon}(\mathbf{w})\, \mathrm{d}\Omega \\ &= \lambda_{\max} \left\|\hat{\boldsymbol{\varepsilon}}(\mathbf{w})\right\|_0^2 \le \lambda_{\max} c_{ac} \left\|\tilde{\boldsymbol{\varepsilon}}(\mathbf{w})\right\|_0^2 \end{aligned} \tag{42}$$

where $\lambda_{\max}$ is the maximum of eigenvalues for elasticity constant matrix $\mathbf{D}$.

In deriving of Eq. (42), we have used (1) the solid is stable and hence the elasticity constant matrix is symmetric positive definite and can always be decomposed into orthogonal matrix $\mathbf{U}$ and diagonal matrix $\boldsymbol{\Lambda}$ of positive eigenvalues; (2) norm preserving property of orthogonal matrix $\mathbf{U}$; (3) the strain norm equivalence: Eq. (22).

On the other hand, using Eq. (4) we have

$$\|\tilde{\boldsymbol{\varepsilon}}(\mathbf{v})\|_0^2 = (\tilde{\boldsymbol{\varepsilon}}, \tilde{\boldsymbol{\varepsilon}})_0 = \left[\frac{\partial v_1}{\partial x_1}\right]^2 + \left[\frac{\partial v_2}{\partial x_2}\right]^2 + \left[\frac{\partial v_1}{\partial x_2} + \frac{\partial v_2}{\partial x_1}\right]^2, \tag{43}$$

$$|\mathbf{v}|_1^2 \equiv \|\nabla\mathbf{v}\|_0^2 = \left[\frac{\partial v_1}{\partial x_1}\right]^2 + \left[\frac{\partial v_2}{\partial x_2}\right] + \left[\frac{\partial v_1}{\partial x_2}\right]^2 + \left[\frac{\partial v_2}{\partial x_1}\right]^2, \tag{44}$$

where $|\mathbf{v}|_1$ represents the semi-norm of vector $\mathbf{v}$. Eq. (43) and Eq. (44) gives

$$\frac{1}{2}\|\tilde{\boldsymbol{\varepsilon}}(\mathbf{v})\|_0^2 \le |\mathbf{v}|_1^2 \le 2\|\tilde{\boldsymbol{\varepsilon}}(\mathbf{v})\|_0^2, \tag{45}$$

which indicates that the semi norm $|\mathbf{v}|$ of the compatible strains is equivalent to norm $\|\tilde{\boldsymbol{\varepsilon}}(\mathbf{v})\|_0$. Therefore, there exists a constant c_ε such that $|\mathbf{v}|_1 = c_\varepsilon \ \|\tilde{\boldsymbol{\varepsilon}}(\mathbf{v})\|_0$.

In addition, from Eq. (37), we can obtain that

$$\|\mathbf{v}\|_1 = |\mathbf{v}|_1 + \|\mathbf{v}\|_0 . \tag{46}$$

Therefore, we have

$$|\mathbf{v}|_1 = c_\varepsilon \ \|\tilde{\boldsymbol{\varepsilon}}(\mathbf{v})\|_0 \le \|\mathbf{v}\|_1 , \tag{47}$$

or

$$\|\tilde{\boldsymbol{\varepsilon}}(\mathbf{v})\|_0 \le \frac{1}{c_\varepsilon}\|\mathbf{v}\|_1 . \tag{48}$$

Hence, from Eq. (42) and Eq. (48) we have

$$|a(\mathbf{w},\mathbf{v})| \le c_U \|\mathbf{w}\|_1 \|\mathbf{v}\|_1 , \tag{49}$$

where $c_U = \lambda_{\max} c_{ac}/c_\varepsilon^2$ is a constant independent of $\mathbf{w}$ and $\mathbf{v}$.

Eq. (49) indicates the bilinear weak form $a(\mathbf{w},\mathbf{v})$ is bounded and hence the x-Galerkin formulation using $a(\mathbf{w},\mathbf{v})$ will be stable.

On the other hand, in a similar way for deriving Eq. (42), we have

$$a(\mathbf{w},\mathbf{w}) \ge \lambda_{\min} c_{ca} \|\tilde{\boldsymbol{\varepsilon}}(\mathbf{w})\|_0^2 , \tag{50}$$

where $\lambda_{\min}$ is the smallest eigenvalue of elasticity constant matrix $\mathbf{D}$.

Note that the Korn's inequality [3] shows that there exist a constant $c_K > 0$ such that

$$\|\tilde{\boldsymbol{\varepsilon}}(\mathbf{w})\|_0 \ge c_K \|\mathbf{w}\|_1 . \tag{51}$$

Hence, Eq. (50) and (51) arrive at

$$a(\mathbf{w},\mathbf{w}) \ge c_L \|\mathbf{w}\|_1^2 \tag{52}$$

where $c_L = \lambda_{\min} c_{ca} c_K^2$ is a constant independent of displacement $\mathbf{w}$.

Note that the above proof is similar to that in [55]. By the Lax-Milgram Theorem [3,4], we complete the proof of Theorem 1. □

When the dimension of the cells approaches to zero, the smoothing strain at a point will approach to compatible strain at that point, and hence the entire constructed strain field will approach to that of the exact strain field. With the existence and uniqueness provided by Theorem 1, we can now have the following Corollary.

Corollary 1 (Convergence) *The solution obtained from the PIM-CS based on the x-Galerkin weak form is convergent to the exact solutions of original strong form when the dimension of the cells approaches zero.*

Equations (49) and (52) give $c_L \|\mathbf{w}\|_1^2 \le |a(\mathbf{w},\mathbf{w})| \le c_U \|\mathbf{w}\|_1^2$ which indicates that the strain energy from PIM-CS solution is bounded from both sides. Therefore, the convergence properties of the x-Galerkin model are determined by those two constants which depend on the choices of smoothing domains.

Corollary 2 *Theorem 1 and its proof procedure show that the smoothing domain for a point can be chosen as desired for various purposes, and it is not limited only to the smoothing domains detailed in Sect. 4.2. Thoughtfully chosen smoothing domains can give solutions with the high accuracy and convergence rates. The key is that strain energy norm for the assumed strain field must be equivalent to that of the compatible strain field.*

5.4 Bound property of strain energy potential for the PIM-CS

Now that we have confirmed both Scheme 1 ($\alpha = 0$) and Scheme 2 ($\alpha = 1$) given in Sect. 4.3 will produce solutions that converge to the exact solution of the original strong form. Both U_{EG} and U_{HR} defined in Eqs. (30) and (31) are thus bounded: $U_{EG}^{\min} \le U_{EG} \le U_{EG}^{\max}$ and $U_{HR}^{\min} \le U_{HR} \le U_{HR}^{\max}$, which implies that

$$U_{\min} \le \alpha U_{EG} + (1-\alpha) U_{HR} \le U_{\max}, \text{ when } 0 \le \alpha \le 1, \quad (53)$$

where $U_{\min} = \min(U_{EG}^{\min}, U_{HR}^{\min})$ and $U_{\max} = \max(U_{EG}^{\max}, U_{HR}^{\max})$. Therefore, we can now assert that the solution of PIM-CS based on Eq. (29) is convergent if $0 \le \alpha \le 1$. However, when we generalize α to a finite real number, we need to establish the following theorem.

Theorem 3 (Generalization of α) *For any finite real number $\alpha \in (-\infty, +\infty)$ the PIM-CS solution based on extended parameterized functional (29) converges to the exact solution of original strong form, when the dimensions of all the background cells approach to zero.*

Proof Equation (29) can be re-written as

$$\hat{\Pi}(\mathbf{v}) = \int_{\Omega} \left\{ \frac{1}{2} \hat{\boldsymbol{\varepsilon}}^{\mathrm{T}}(\mathbf{v}) \mathbf{D} \hat{\boldsymbol{\varepsilon}}(\mathbf{v}) + (1-\alpha) \left[\hat{\boldsymbol{\varepsilon}}^{\mathrm{T}}(\mathbf{v}) \mathbf{D} \tilde{\boldsymbol{\varepsilon}}(\mathbf{v}) - \hat{\boldsymbol{\varepsilon}}^{\mathrm{T}}(\mathbf{v}) \mathbf{D} \hat{\boldsymbol{\varepsilon}}(\mathbf{v}) \right] - \mathbf{v}^{\mathrm{T}} \mathbf{b} \right\} \mathbf{d}\Omega - \int_{\Gamma_t} \mathbf{v}^{\mathrm{T}} \mathbf{T} \mathrm{d}\Gamma \quad (54)$$

When the dimensions of all the background cells approach to zero, the locally smoothed strains at these vertices of each of the triangular subdomains $\Omega_{k,i}$ will approach to the compatible strain $\tilde{\boldsymbol{\varepsilon}}$ and thus

$$\int_{\Omega} [\hat{\boldsymbol{\varepsilon}}^{\mathrm{T}}(\mathbf{v}) \mathbf{D} \tilde{\boldsymbol{\varepsilon}}(\mathbf{v}) - \hat{\boldsymbol{\varepsilon}}^{\mathrm{T}}(\mathbf{v}) \mathbf{D} \hat{\boldsymbol{\varepsilon}}(\mathbf{v})] \mathbf{d}\Omega \to 0. \quad (55)$$

At this limit, Eq. (55) becomes simply the proven x-Galerkin formulation. This completes the proof of Theorem 2. □

Theorem 3 ensures that PIM-CS solution will converge for any finite real number $\alpha \in (-\infty, +\infty)$. In other words, the convergence of PIM-CS is independent of α. However, the convergence rate and bound properties are effected by the choice of α, and therefore we do not usually want to use a too big α. An ideal α is that can give us the exact solution in energy norm, but it can be expensive to obtain. An often preferred α is that can produce a solution very close to the exact solution, or gives us a "tight" solution bounds, which is further stated in the following theorem.

Theorem 4 (Bound properties) *For any assumed linear displacement field $\mathbf{v}$ in a Hilbert space, the strains at any point within $\Omega_{k,i}$ are obtained using Eq. (17); and Eq. (29) is used to produce the discretized system equation. Then, there exists an $\alpha_0 \in [-\frac{3}{2}, -\frac{1}{2}]$ and an $\alpha_1 \in [\frac{3}{2}, \frac{5}{2}]$ such that*

(1) $\overline{U}(\mathbf{v}) \le \hat{U}(\mathbf{v}) \le \tilde{U}(\mathbf{v})$, *when* $\alpha \in [\alpha_0, \alpha_1]$;
(2) $\hat{U}(\mathbf{v}) = \overline{U}(\mathbf{v})$, *when* $\alpha = \alpha_1$;
(3) $\hat{U}(\mathbf{v}) = \tilde{U}(\mathbf{v})$, *when* $\alpha = \alpha_0$;

where $\hat{U}(\mathbf{v})$ is the strain energy obtained using the PIM-CS assumed strain field:

$$\hat{U}(\mathbf{v}) = \sum_{k=1}^{N} \sum_{i=1}^{M} \left\{ \frac{1}{2} \int_{\Omega_{k,i}} \hat{\boldsymbol{\varepsilon}}_{k,i}^{\mathrm{T}}(\mathbf{v}) \mathbf{D} \hat{\boldsymbol{\varepsilon}}_{k,i}(\mathbf{v}) d\Omega + (1-\alpha) \int_{\Omega_{k,i}} \hat{\boldsymbol{\varepsilon}}_{k,i}^{\mathrm{T}}(\mathbf{v}) \mathbf{D} \left[\tilde{\boldsymbol{\varepsilon}}_{k,i}(\mathbf{v}) - \hat{\boldsymbol{\varepsilon}}_{k,i}(\mathbf{v}) \right] d\Omega \right\}, \quad (56)$$

$\tilde{U}(\mathbf{v})$ is the strain energy of the compatible strain field of the FEM model:

$$\tilde{U}(\mathbf{v}) = \sum_{k=1}^{N} \sum_{i=1}^{M} \frac{1}{2} \int_{\Omega_{k,i}} \tilde{\boldsymbol{\varepsilon}}_{k,i}^{\mathrm{T}}(\mathbf{v}) \mathbf{D} \tilde{\boldsymbol{\varepsilon}}_{k,i}(\mathbf{v}) \mathbf{d}\Omega \quad (57)$$

and $\overline{U}(\mathbf{v})$ is the strain energy of the smoothed strain field of the NS-PIM model:

$$\overline{U}(\mathbf{v}) = \sum_{k=1}^{N} \frac{1}{2} \int_{\Omega_k} \bar{\boldsymbol{\varepsilon}}_k^{\mathrm{T}}(\mathbf{v}) \mathbf{D} \bar{\boldsymbol{\varepsilon}}_k(\mathbf{v}) \mathbf{d}\Omega \quad (58)$$

Proof When the linear interpolation for the displacement field is used, the compatible strain $\mathbf{L}_{\mathrm{d}}\mathbf{v}$ is constant in each of the background triangles. Hence, the strain $\boldsymbol{\varepsilon}_I$ in Eq. (19) is in fact the compatible strain, because the smoothing over a constant field will have no effect. Furthermore, the strains $\breve{\boldsymbol{\varepsilon}}_P$ from (20) in sub-triangular domain $\Omega_{k,i}$ can be written as

$$\breve{\boldsymbol{\varepsilon}}_{kP,\,i} = \frac{1}{A_{kP,\,i}} \int_{\Omega_{kP,\,i}} \mathbf{L}_{\mathbf{d}} \hat{\mathbf{u}}(\mathbf{x}) \, \mathrm{d}\Omega, \quad (59)$$

in which $\Omega_{kP,i} = \Omega_{k,2i-1} + \Omega_{k,2i}$, $i = 1, 2, \ldots, M/2$ (see Figs. 2, 3).

To evaluate the strain energy in the entire problem domain, we define

$$\begin{aligned} \omega_{k,\,i} &\equiv \textstyle\int_{\Omega_{k,i}} \hat{\boldsymbol{\varepsilon}}_{k,\,i}^{\mathrm{T}}(\mathbf{v}) \mathbf{D} \hat{\boldsymbol{\varepsilon}}_{k,\,i}(\mathbf{v}) \, \mathrm{d}\Omega, \\ \pi_{k,\,i} &\equiv \textstyle\int_{\Omega_{k,\,i}} \hat{\boldsymbol{\varepsilon}}_{k,\,i}^{\mathrm{T}}(\mathbf{v}) \mathbf{D} \tilde{\boldsymbol{\varepsilon}}_{k,\,i}(\mathbf{v}) \mathrm{d}\Omega. \end{aligned} \quad (60)$$

Note that the strain at any point within the sub-domain $\Omega_{k,i}$ can be written as

$$\hat{\boldsymbol{\varepsilon}}_{k,\,i} = L_1(\mathbf{x}) \bar{\boldsymbol{\varepsilon}}_k + L_2(\mathbf{x}) \breve{\boldsymbol{\varepsilon}}_{kP,\,i} + L_3(\mathbf{x}) \tilde{\boldsymbol{\varepsilon}}_{k,\,i}, \quad (61)$$

where $\bar{\boldsymbol{\varepsilon}}_k$, $\breve{\boldsymbol{\varepsilon}}_{kP,\,i}$ and $\tilde{\boldsymbol{\varepsilon}}_{k,\,i}$ are defined by Eqs. (19)–(21).

Using Eq. (61), we have

$$\omega_{k,\,i} = \int_{\Omega_{k,\,i}} \sum_{\beta=1}^{3} [L_\beta(\mathbf{x})\mathbf{e}_{k,\beta}]^{\mathrm{T}}\mathbf{D} \sum_{\gamma=1}^{3} [L_\gamma(\mathbf{x})\mathbf{e}_{k,\gamma}]\,\mathrm{d}\Omega$$
$$= \sum_{\beta,\gamma=1}^{3} \mathbf{e}_{k,\beta}^{\mathrm{T}}\mathbf{D}\mathbf{e}_{k,\gamma} \int_{\Omega_{k,\,i}} L_\beta(\mathbf{x})L_\gamma(\mathbf{x})\mathrm{d}\Omega \tag{62}$$

and

$$\omega_{k,i+1} = \int_{\Omega_{k,\,i+1}} \sum_{\beta=1}^{3} [L_\beta(\mathbf{x})\kappa_{k,\beta}]^{\mathrm{T}}\mathbf{D} \sum_{\gamma=1}^{3} [L_\gamma(\mathbf{x})\kappa_{k,\gamma}]\,\mathrm{d}\Omega$$
$$= \sum_{\beta,\gamma=1}^{3} \kappa_{k,\beta}^{\mathrm{T}}\mathbf{D}\kappa_{k,\gamma} \int_{\Omega_{k,\,i+1}} L_\beta(\mathbf{x})L_\gamma(\mathbf{x})\mathrm{d}\Omega \tag{63}$$

where $\mathbf{e}_{k,1} = \overline{\boldsymbol{\varepsilon}}_k$, $\mathbf{e}_{k,2} = \breve{\boldsymbol{\varepsilon}}_{kP,\,i}$, $\mathbf{e}_{k,3} = \widehat{\boldsymbol{\varepsilon}}_{k,\,i}$, $\kappa_{k,1} = \overline{\boldsymbol{\varepsilon}}_k$, $\kappa_{k,2} = \breve{\boldsymbol{\varepsilon}}_{kP,\,i+1}$ and $\kappa_{k,3} = \widehat{\boldsymbol{\varepsilon}}_{k,\,i+1}$.

Using the formula [2,59]

$$\int_A L_1^p L_2^q L_3^r \mathrm{d}A = \frac{p!q!r!}{(p+q+r+2)!}2A, \tag{64}$$

we have

$$\sum_{i=1,3,\ldots}^{M-1} [\omega_{k,\,i} + \omega_{k,\,i+1}]$$
$$= \sum_{i=1,3,\ldots}^{M-1} \sum_{\beta,\gamma=1}^{3} \left[\mathbf{e}_{k,\beta}^{\mathrm{T}}\mathbf{D}\mathbf{e}_{k,\gamma} \int_{\Omega_{k,\,i}} L_\beta(\mathbf{x})L_\gamma(\mathbf{x})\mathrm{d}\Omega \right.$$
$$\left. + \kappa_{k,\beta}^{\mathrm{T}}\mathbf{D}\kappa_{k,\gamma} \int_{\Omega_{k,\,i+1}} L_\beta(\mathbf{x})L_\gamma(\mathbf{x})\mathrm{d}\Omega \right] \tag{65}$$
$$= \frac{1}{6}\left[3\overline{\Theta}(\mathbf{v}) + 2\breve{\Theta}(\mathbf{v}) + \tilde{\Theta}(\mathbf{v})\right]$$

where $\overline{\Theta}(\mathbf{v}) = A_k\overline{\boldsymbol{\varepsilon}}_k^{\mathrm{T}}\mathbf{D}\overline{\boldsymbol{\varepsilon}}_k$, $\breve{\Theta}(\mathbf{v}) = \sum_{i=1}^{M/2} A_{kP,\,i}\breve{\boldsymbol{\varepsilon}}_{kP,\,i}^{\mathrm{T}}\mathbf{D}\breve{\boldsymbol{\varepsilon}}_{kP,\,i}$, and $\tilde{\Theta}(\mathbf{v}) = \sum_{i=1}^{M} A_{k,\,i}\tilde{\boldsymbol{\varepsilon}}_{k,\,i}^{\mathrm{T}}\mathbf{D}\tilde{\boldsymbol{\varepsilon}}_{k,\,i}$.

Similarly, we have

$$\sum_{i=1,3,\ldots}^{M-1} (\pi_{k,\,i} + \pi_{k,\,i+1}) = \frac{1}{3}\left[\overline{\Theta}(\mathbf{v}) + \breve{\Theta}(\mathbf{v}) + \tilde{\Theta}(\mathbf{v})\right]. \tag{66}$$

Substituting Eqs. (65), (66) into (56) yields,

$$\hat{U}_k(\mathbf{v}) = \frac{1}{12}\left[(2\alpha+1)\overline{\Theta}(\mathbf{v}) + 2\breve{\Theta}(\mathbf{v}) + (3-2\alpha)\tilde{\Theta}(\mathbf{v})\right]. \tag{67}$$

In addition, the positivity of $\mathbf{D}$ gives

$$\int_{\Omega_k} (\overline{\boldsymbol{\varepsilon}}_k - \tilde{\boldsymbol{\varepsilon}}_{k,\,i})^{\mathrm{T}}\mathbf{D}(\overline{\boldsymbol{\varepsilon}}_k - \tilde{\boldsymbol{\varepsilon}}_{k,\,i})\mathrm{d}\Omega$$
$$= \sum_{i=1}^{M} \int_{\Omega_{k,\,i}} (\overline{\boldsymbol{\varepsilon}}_k - \tilde{\boldsymbol{\varepsilon}}_{k,\,i})^{\mathrm{T}}\mathbf{D}(\overline{\boldsymbol{\varepsilon}}_k - \tilde{\boldsymbol{\varepsilon}}_{k,\,i})\mathrm{d}\Omega$$
$$= \sum_{i=1}^{M} \left[A_{k,\,i}\overline{\boldsymbol{\varepsilon}}_k^{\mathrm{T}}\mathbf{D}\overline{\boldsymbol{\varepsilon}}_k - 2A_{k,\,i}\overline{\boldsymbol{\varepsilon}}_k^{\mathrm{T}}\mathbf{D}\tilde{\boldsymbol{\varepsilon}}_{k,\,i} + A_{k,\,i}\tilde{\boldsymbol{\varepsilon}}_{k,\,i}^{\mathrm{T}}\mathbf{D}\tilde{\boldsymbol{\varepsilon}}_{k,\,i} \right]$$
$$= -A_k\overline{\boldsymbol{\varepsilon}}_k^{\mathrm{T}}\mathbf{D}\overline{\boldsymbol{\varepsilon}}_k + \sum_{i=1}^{M} A_{k,\,i}\tilde{\boldsymbol{\varepsilon}}_{k,\,i}^{\mathrm{T}}\mathbf{D}\tilde{\boldsymbol{\varepsilon}}_{k,\,i} \geq 0 \tag{68}$$

and thus

$$\sum_{i=1}^{M} A_{k,\,i}\tilde{\boldsymbol{\varepsilon}}_{k,\,i}^{\mathrm{T}}\mathbf{D}\tilde{\boldsymbol{\varepsilon}}_{k,\,i} \geq A_k\overline{\boldsymbol{\varepsilon}}_k^{\mathrm{T}}\mathbf{D}\overline{\boldsymbol{\varepsilon}}_k. \tag{69}$$

Similarly, we have

$$\sum_{i=1}^{M} A_{k,i}\tilde{\boldsymbol{\varepsilon}}_{k,i}^{\mathbf{T}}\mathbf{D}\tilde{\boldsymbol{\varepsilon}}_{k,i} \geq \sum_{i=1}^{M/2} A_{kP,i}\breve{\boldsymbol{\varepsilon}}_{kP,i}^{\mathrm{T}}\mathbf{D}\breve{\boldsymbol{\varepsilon}}_{kP,i} \geq A_k\overline{\boldsymbol{\varepsilon}}_k^{\mathrm{T}}\mathbf{D}\overline{\boldsymbol{\varepsilon}}_k, \tag{70}$$

or

$$\tilde{\Theta} \geq \breve{\Theta} \geq \overline{\Theta}. \tag{71}$$

It follows from Eq. (67) that

$$\sum_{k=1}^{N} \left[\hat{U}_k(\mathbf{v}) - \frac{1}{2}\sum_{i=1}^{M} A_{k,\,i}\tilde{\boldsymbol{\varepsilon}}_{k,\,i}^{\mathbf{T}}\mathbf{D}\tilde{\boldsymbol{\varepsilon}}_{k,\,i} \right]$$
$$= \frac{1}{12}\sum_{k=1}^{N} \left[(2\alpha+1)\overline{\Theta}(\mathbf{v}) - (2\alpha+3)\tilde{\Theta}(\mathbf{v}) + 2\breve{\Theta}(\mathbf{v}) \right] \tag{72}$$

Substituting (71) into (72) gives $\hat{U}(\mathbf{v}) \leq \tilde{U}(\mathbf{v})$ when $\alpha \geq -\frac{1}{2}$, and $\hat{U}(\mathbf{v}) \geq \tilde{U}(\mathbf{v})$ when$\alpha \leq -\frac{3}{2}$. Hence, there exist an $\alpha_0 \in [-\frac{3}{2}, -\frac{1}{2}]$ such that $\hat{U}(\mathbf{v}) = \tilde{U}(\mathbf{v})$ when $\alpha = \alpha_0$, which implies that the strain energy obtained from PIM-CS is exactly the same as that of the FEM model.

Similarly, From Eq. (67) we also have

$$\sum_{k=1}^{N} \left[\hat{U}_k(\mathbf{v}) - \frac{1}{2}A_k\overline{\boldsymbol{\varepsilon}}_k^{\mathrm{T}}\mathbf{D}\overline{\boldsymbol{\varepsilon}}_k \right]$$
$$= \frac{1}{12}\sum_{k=1}^{N} \left[(2\alpha-5)\overline{\Theta}(\mathbf{v}) + 2\breve{\Theta}(\mathbf{v}) + (3-2\alpha)\tilde{\Theta}(\mathbf{v}) \right] \tag{73}$$

Substituting Eq. (71) into (73) gives $\hat{U}(\mathbf{v}) \geq \overline{U}(\mathbf{v})$when $\alpha \leq \frac{3}{2}$, and $\hat{U}(\mathbf{v}) \leq \overline{U}(\mathbf{v})$ when$\alpha \geq \frac{5}{2}$. Therefore, there exist an $\alpha_1 \in [\frac{3}{2}, \frac{5}{2}]$ such that $\hat{U}(\mathbf{v}) = \overline{U}(\mathbf{v})$ when $\alpha = \alpha_1$, which implies that the strain energy obtained from PIM-CS is exactly the same as that of the NS-PIM model. This completes the proof. □

Theorem 3 shows that the strain energy obtained from the PIM-CS model is exactly the same as that from NS-PIM and FEM when $\alpha = \alpha_1$ and $\alpha = \alpha_0$, respectively. This leads to the following Corollary.

Corollary 3 *The PIM-CS produces the lower bound solution in energy norm when α is near α_0, and the upper bound solution when α is near α_1.*

Substituting Eq. (67) into (29), and then the stationary condition of (29) gives

$$\hat{\mathbf{K}} = \frac{1}{12}\sum_{k=1}^{N}\left[(2\alpha+1)A_k\overline{\mathbf{B}}_k^{\mathrm{T}}\mathbf{D}\overline{\mathbf{B}}_k + 2\sum_{i=1}^{M/2}A_{kP,i}\breve{\mathbf{B}}_{kP,i}^{\mathrm{T}}\mathbf{D}\breve{\mathbf{B}}_{kP,i} + (3-2\alpha)\sum_{i=1}^{M}A_{k,i}\tilde{\mathbf{B}}_{k,i}^{\mathrm{T}}\mathbf{D}\tilde{\mathbf{B}}_{k,i}\right], \tag{74}$$

which results in the following Corollary:

Corollary 4 *The stiffness matrix $\hat{\mathbf{K}}$ obtained from PIM-CS is symmetric.*

Corollary 5 *When the conditions of Theorem 3 are satisfied and the same mesh is used, the strain energy obtained using the PIM-CS is no-less than that from the FEM solution based on the standard Galerkin weak form, and no-larger than the strain energy from the NS-PIM solution, namely: $\frac{1}{2}\tilde{\mathbf{d}}^{\mathrm{T}}\tilde{\mathbf{K}}\tilde{d} \le \frac{1}{2}\hat{\mathbf{d}}^{\mathrm{T}}\hat{\mathbf{K}}\hat{d} \le \frac{1}{2}\overline{\mathbf{d}}^{\mathrm{T}}\overline{\mathbf{K}}\,\overline{\mathbf{d}}$.*

The proof of Corollary 5 is similar to that in [30,49], thus is omitted.

Remark 1 It is clear from the proof process of Theorem 3 that when PIM shape functions with polynomial bases are used, exact integration is readily available and no numerical integration is needed.

The above theoretical analysis and discussions show that the PIM-CS has the following features: (1) the distribution of the strain $\hat{\boldsymbol{\varepsilon}}$ (thus stress $\hat{\sigma}$) in PIM-CS is continuous in the entire domain Ω; (2) PIM-CS can produce linear displacement field exactly using a sufficient large interval for α, and hence can pass the standard path test; (3) when 3-node triangular mesh that can be generated automatically is used, and no numerical integration is needed; (4) the stiffness matrix for the PIM-CS is symmetric and of the same size of the FEM model using the same mesh; (5) PIM-CS can provide the upper bound and lower bound solution of exact solution by adjusting parameter α; (6) there exists a value of $\alpha \in (\alpha_0, \alpha_1)$ such that PIM-CS solution is ultra accurate and of superconvergence.

6 Superconvergence of the PIM-CS

In the error analysis for FEM based on the minimum total potential principle, the determination of the upper bound of $\|u-u_h\|_m$ is usually reduced to the estimation of $\|u-\Pi_h u\|_m$ [60]. Based on the approximation theory, we have

$$\|\mathbf{u}-\Pi_h\mathbf{u}\|_m \le Ch^{n+1-m}\,\|\mathbf{u}\|_{n+1} \tag{75}$$

In general this estimate can not be improved even if the solution $\mathbf{u}$ possesses a higher smoothness. Therefore,

$$\|\mathbf{u}-\Pi_h\mathbf{u}\|_m = O(h^{n+1-m}) \tag{76}$$

is the optimal order error estimate.

By "optimal" we mean that the rate of convergence *cannot* be improved, and the rates are also called theoretical rates. For linear FEM, the optimal theoretical rate is 2.0 for the displacement norm, and 1.0 for the strain energy norm. It is known, that this fact does not exclude the possibility that the approximation of the derivatives may be of higher order accuracy at some special points, called superconvergence points. This means that one can find points in the elements, where the rate of convergence for the strain energy is more than 1.0 and less than 2.0, and this is confirmed in FEM models [1,60]. However, for the displacement, the theoretical value of 2.0 still cannot be improved when the compatible strain field is used to compute the stiffness matrix (fully compatible).

We will show in Sect. 7 that the SC-PIM has a special superconvergent property that behaves very differently from the fully compatible FEM models. The SC-PIM is equipped with an adjustable parameter α. Both the displacement field $\hat{\mathbf{u}}(\alpha)$ and strain field $\hat{\boldsymbol{\varepsilon}} = (\hat{\mathbf{u}}(\alpha);\alpha)$ are the functions of α. Therefore, an adjustment on α can obviously influence the accuracy and convergence of solutions in *both* displacement and strain energy norms. When α is properly tuned, the SC-PIM can produce a convergence rate that far exceeds the so-called theoretical optimal values for in both measures of displacement and strain energy norms: a truly superconvergence. Furthermore, from Theorem 3 we know that the solution of the PIM-CS for a α near to $\alpha_0 \in [-3/2, -1/2]$ is a lower bound of the exact solution in energy norm; while for that one near to $\alpha_1 \in [3/2, 5/2]$, it is an upper bound. Thus, there exists a value of $\alpha_{exact} \in (\alpha_0, \alpha_1)$ at which the strain energy is the exact solution. This implies that we should be able to obtain the "exact" solution using a PIM-CS model of finite dimension! This opens an opportunities for establishing extremely fast convergence models producing ultra accurate solutions, even liner displacement fields are used.

In practice, however, it is difficult to find the α_{exact} for a general problem. However, when an $\alpha \approx \alpha_{\text{exact}}$ can be found, the superconvergence property can be found for solutions in both the strain energy and the displacement. In the next section, we will show numerical examples that such an

$\alpha \approx \alpha_{\text{exact}} \in (\alpha_0, \alpha_1)$ can be found for PIM-CS to achieve ultra accurate and superconvergent solutions.

7 Numerical examples

In this section, a number of numerical examples will be examined using the PIM-CS with both linear and quadratic interpolations, referred as linear PIM-CS and quadratic PIM-CS. To investigate quantitatively the numerical results, the error indicators in both displacement and energy norms are defined as follows,

$$E_d = \sqrt{\frac{\sum_{i=1}^{n}\left(u_i^{\text{ref}} - u_i^{\text{num}}\right)^2}{\sum_{i=1}^{n}\left(u_i^{\text{ref}}\right)^2}}, \tag{77}$$

$$E_e = \sqrt{\frac{|U_{\text{num}} - U_{\text{ref}}|}{U_{\text{ref}}}} \tag{78}$$

where the superscript ref denotes the reference or analytical solution, num denotes a numerical solution obtained using a numerical method. To demonstrate the energy bound properties of the PIM-CS numerically, strain energy will be calculated using Eq. (56).

7.1 Standard path test

For a numerical method working for solid mechanics problems, the sufficient requirement for convergence is to pass the standard path test [1]. Therefore, the first example is the standard path test using the present PIM-CS. A rectangular patch of 10×50 is considered, and the displacements are prescribed on all outside boundaries by the following linear function.

$$\begin{cases} u_x = 0.6x \\ u_y = 0.6y \end{cases} \tag{79}$$

The patch is represented using nodes shown in Fig. 4 and error E_d obtained using linear PIM-CS for some α are illustrated in Table 1. It shows that all these errors are less than 1.0×10^{-13} even for $\alpha = \pm 30$. This example verifies numerically Theorem 2 and indicates that the PIM-CS for an arbitrary α can pass the standard path test, and is at least linearly conforming.

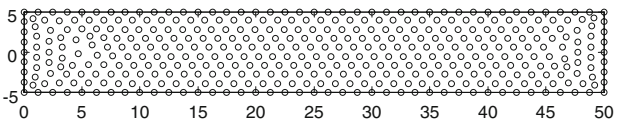

Fig. 4 Node distributions for the standard patch test

7.2 Cantilever 2D solid

A 2D cantilever solid with length $L = 50$m and height $D = 10$m is now studied. The solid is subjected to a parabolic traction at the right end as shown in Fig. 5. Analytical solutions can be found in [61]. The cantilever is studied as a plane stress problem with $E = 3.0 \times 10^7$ Pa, $P = -1,000$ N and $v = 0.3$.

We first numerically investigate the continuity of stress solution obtained using the linear PIM-CS. Figures 6, 7, 8 show the stress distribution of σ_{xx} in a perspective view and projected view on the $x - \sigma_{xx}$ plane. These figures are generated without any post-processing or post-smoothing operations. It is found that the stress σ_{xx} using the PIM-CS is continuous in the entire problem domain, and is very close to the exact solution.

The strain field $\hat{\boldsymbol{\varepsilon}}$ is continuous in entire problem domain. It is, however, not smooth on the interfaces of the sub-domains $\Omega_{k,i}$ as shown in Fig. 7. The stress field from FEM solution is not continuous on the interfaces of the background cells which results in some jumps as shown in Fig. 8. Figure 9 shows that difference of stress distribution σ_{xx} between the different methods. It is seen that the stress distribution from PIM-CS is very close to the exact solution.

Stress solutions for σ_{xy} obtained using FEM, NS-PIM, and PIM-CS are shown in Figs. 10, 11, 12, 13. It is seen again that PIM-CS produces continuous stress in the entire problem domain with high accuracy. The convergence in strain energy obtained using linear PIM-CS is computed and plotted in Fig. 14. It is clear that PIM-CS produces upper and lower bound solutions of the exact solution. Furthermore, the strain energy of these PIM-CS models is in between the compatible FEM and the NS-PIM solutions. These findings verify numerically Theorem 4.

Using Eq. (77) and Eq. (78), errors in displacement and energy norms are computed and plotted in Figs. 15 and 16. When $\alpha = 0.855$, the convergence rate of 3.08 in displacement norm is found, which is much higher than the theoretical value of 2.0 for linear FEM. The convergence rate in energy norm is found as high as 1.88 when $\alpha = 0.855$, as shown in Fig. 16, which is much higher than the theoretical value of 1.0 for linear FEM. These numerical results indicate that PIM-CS is superconvergent not only in energy norm but also in displacement norm for a properly chosen α.

In order to investigate the effect of mesh irregularity on the solution, we examine the convergence of PIM-CS using very irregular meshes shown in Fig. 17. The convergent rates in displacement and energy norm are plotted in Figs. 18 and 19, respectively. It is seen that the PIM-CS can still produce highly accurate and even superconvergent solution for very

Table 1 Standard patch test results obtained using linear PIM-CS with different α

$\alpha(E_d)$	Displacement error (E_d)	α	Displacement error
-30	$0.22170755 \times 10^{-13}$	30	$0.89707588 \times 10^{-13}$
-5	$0.84925581 \times 10^{-14}$	5	$0.16721789 \times 10^{-13}$
$-\frac{3}{2}$	$0.30384429 \times 10^{-14}$	$\frac{5}{2}$	$0.26000885 \times 10^{-13}$
$-\frac{1}{2}$	$0.37677106 \times 10^{-14}$	$\frac{3}{2}$	$0.87468524 \times 10^{-15}$
0	$0.15347691 \times 10^{-14}$	1	$0.21982730 \times 10^{-14}$
Randomly chosen -15.8723	$0.29775149 \times 10^{-13}$	Randomly chosen 9.8233	$0.54424715 \times 10^{-13}$

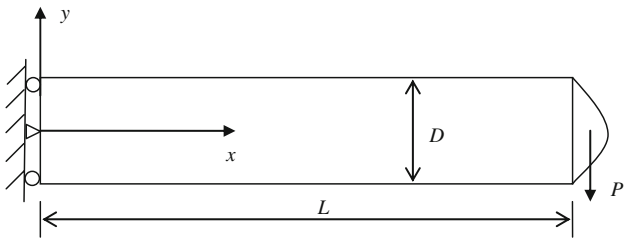

Fig. 5 A 2D cantilever solid subjected to a parabolic traction on the right edge

irregular meshes, showing the robustness of PIM-CS to mesh irregularity.

We note that the linear PIM-CS based on the x-Galerkin weak form ($\alpha = 1$) can produce very accurate solution, which is one-order higher than that from linear FEM and linear NS-PIM. Furthermore, the convergence rates are much higher than the theoretical values for linear FEM: the extended Galerkin model is of superconvergence.

7.3 Infinite 2D solid with a circular hole

An infinite 2D solid with a central circular hole ($a = 1$m) and subjected to a unidirectional tensile ($T_x = 10\,\mathrm{N/m}$) is studied. Owing to its two-fold symmetry, one quarter is modeled with $b = 5$m (as shown in Fig. 20). Symmetry conditions are imposed on the left and bottom edges of the quarter model, and the inner boundary of the hole is traction free. For this benchmark problem, the analytical solution can be found in [61].

To study the convergence of the PIM-CS solution, the strain energy obtained using linear PIM-CS is first computed and plotted in Fig. 21. It is found that PIM-CS can produce upper and lower bounds of the exact solution for different α. Furthermore, the strain energy for these models lies in between those of the compatible FEM and the NS-PIM solutions. These findings verify numerically again Theorem 3.

Using Eqs. (77) and (78), errors in displacement and energy norms are computed and plotted in Figs. 22 and 23. It can be found that the convergence rates in displacement norm is about 2.4 when $\alpha = 0.85$, and 2.19 in energy norm when $\alpha = 1.1$, which are much higher than the theoretical values. Superconvergence occurs at $\alpha = 0.85$ in displacement norm, and at $\alpha = 1.1$ in energy norm.

The linear PIM-CS based on the x-Galerkin weak form ($\alpha = 1$) can also produce very high accurate solution, which is one-order higher accurate than that of linear FEM and NS-PIM solutions. A superconvergence rate of 1.42 in energy norm is also found.

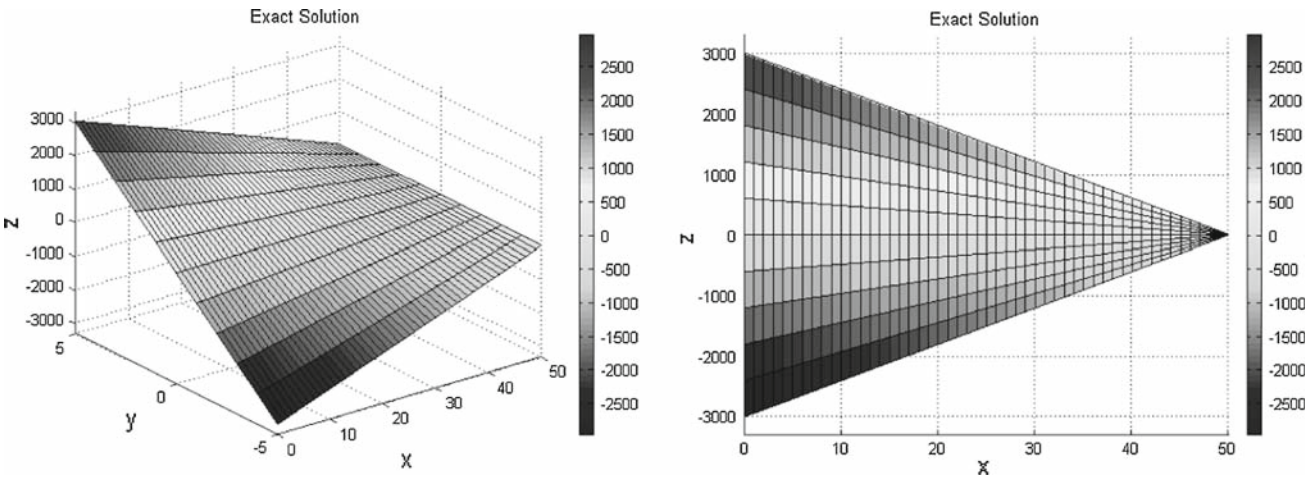

Fig. 6 Distribution of stress σ_{xx} of the exact solution

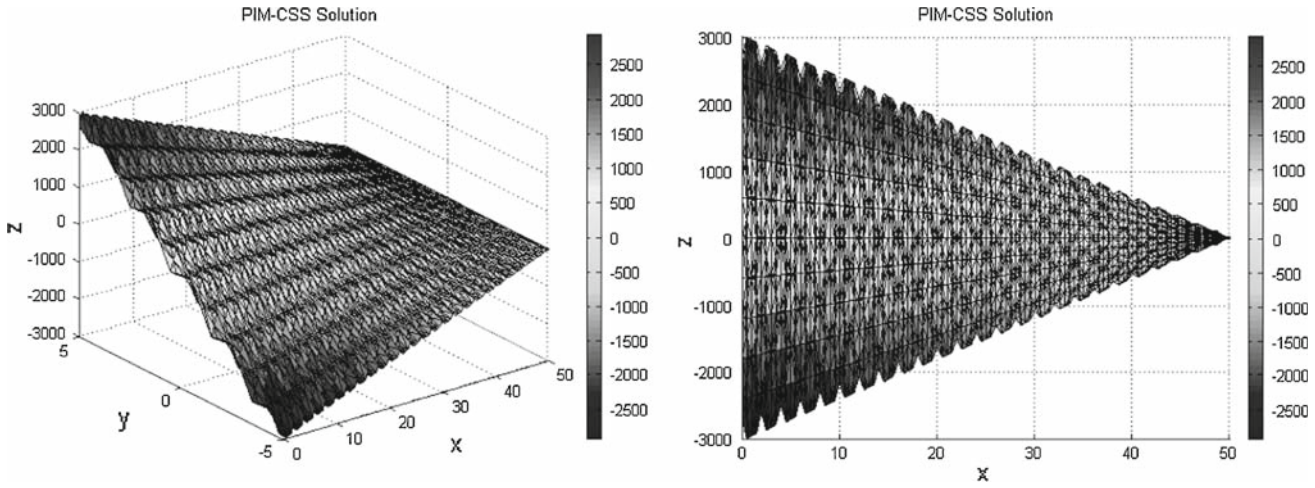

Fig. 7 Distribution of stress σ_{xx} of the PIM-CS solution. These figures are generated without any post-smoothing operations. It is clear that the PIM-CS solution is continuous in the entire problem domain, but not very smooth

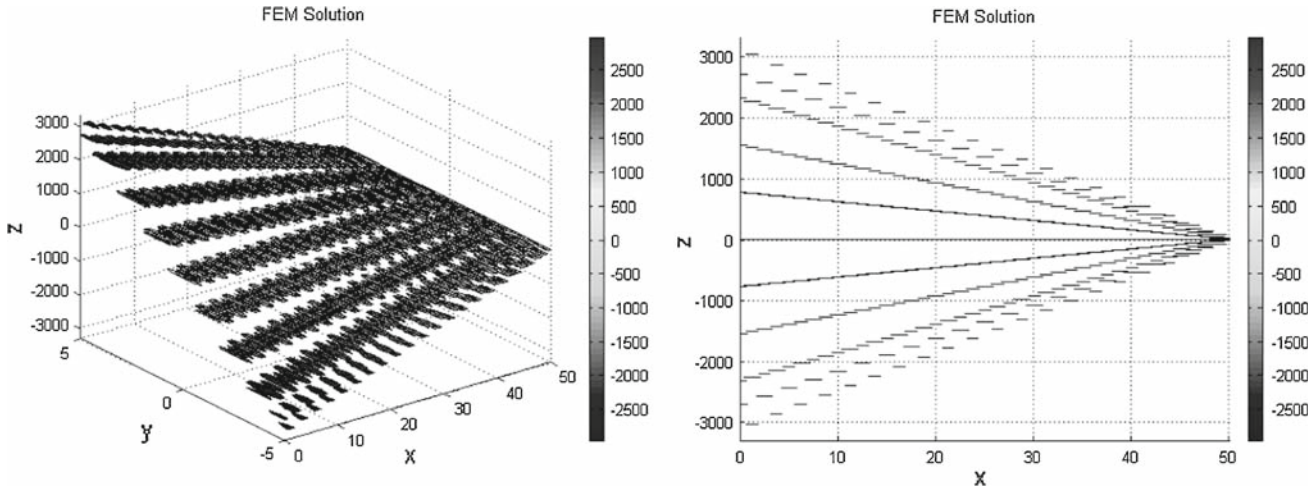

Fig. 8 Distribution of stress σ_{xx} of the FEM solution. These figures are generated without any post-processing or post-smoothing operations. It is clear that the stress from FEM solution is discontinuous and has jumps

7.4 Square solid subjected to uniform pressure and body force

A 2D square solid with body force of $\mathbf{b}^{\mathrm{T}} = \{0, -1\}$ is now studied, as shown in Fig. 24. The solids are constrained on the left, the right, and the bottom edges, and subjected to uniform pressure along the top edge. The problem is considered as plane stress with $\upsilon = 0.3$ and $\mathrm{E} = 3.0 \times 10^7$ Pa.

The convergence property and energy bound for linear PIM-CS are also investigated in similar ways as in the previous examples. As the analytical solution is not available for this problem, the reference solution of strain energy is obtained using the FEM with a very fine mesh. The computed strain energy and convergence rate in energy norm are plotted in Figs. 25 and 26, respectively. It is seen again that the linear PIM-CS produced very accurate solution and superconvergent solution in energy norm with a convergent rate of 1.4 when $\alpha = 1$ and 1.89 when $\alpha = 1.05$, respectively.

7.5 An L-shaped component

An elastic L-shaped component subjected to a pressure load is shown in Fig. 27. Plane stress condition is assumed and the reference solution of strain energy is obtained using FEM with a very fine mesh. The convergence and energy bound for linear PIM-CS are investigated in similar ways as in the previous examples. The computed strain energy and convergent rate in energy norm for different α are plotted in Figs. 28

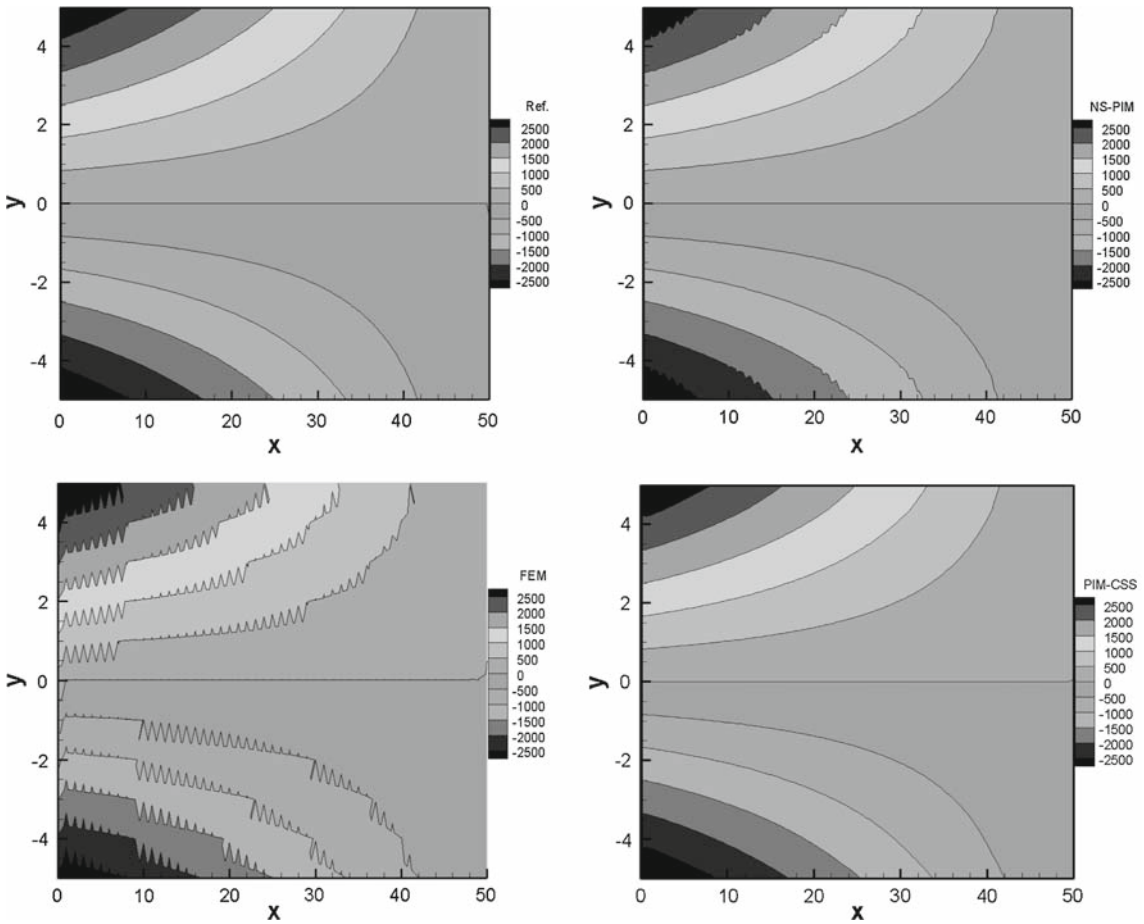

Fig. 9 Contour plots of stress σ_{xx} obtained using different numerical methods. It is clear that the PIM-CS solution is very close to the exact one

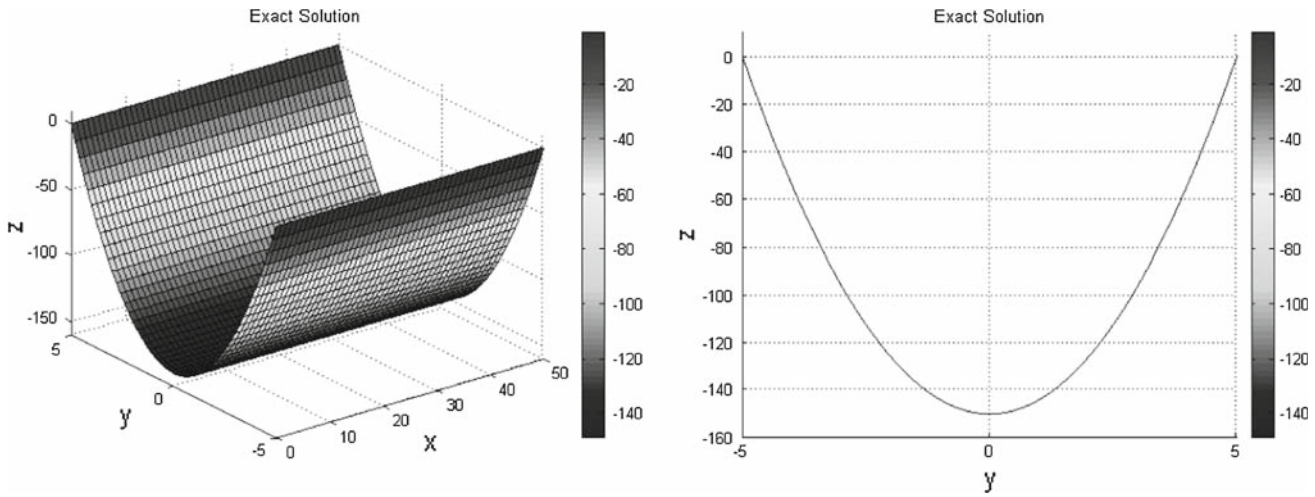

Fig. 10 Stress σ_{xy} distribution of the exact solution

and 29, respectively. It is found that the accuracy of linear PIM-CS is very high in energy norm when $\alpha = 1$, which about 10 times more accurate than that of linear FEM using the same mesh. Furthermore, the superconvergence is also found: convergent rates in energy norm is 1.35 when $\alpha = 1$; and 1.85 when $\alpha = 0.95$.

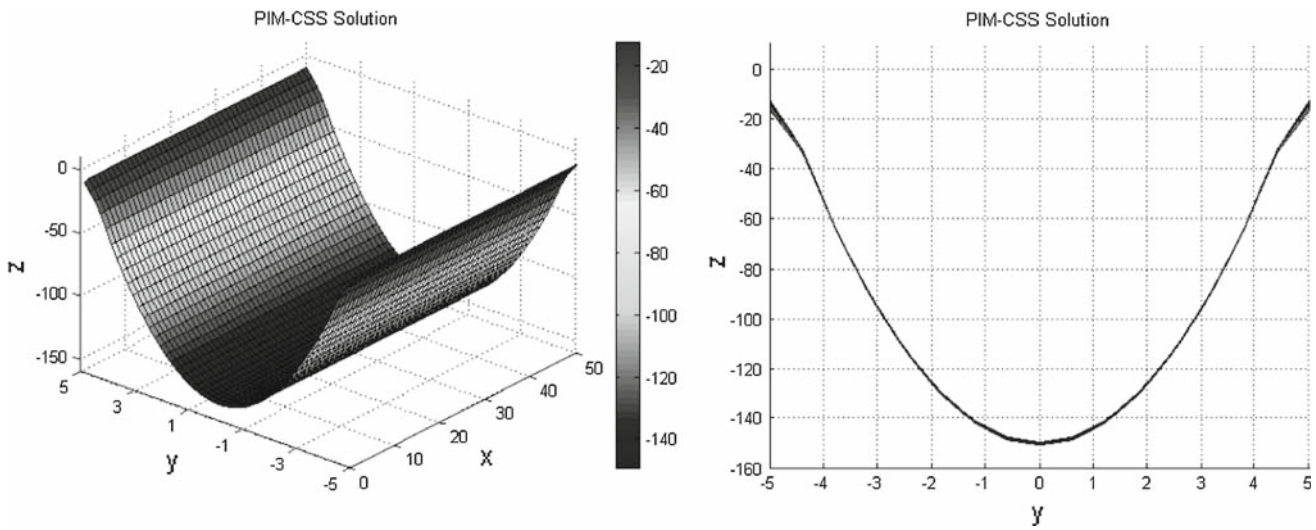

Fig. 11 Stress σ_{xy} distribution of the PIM-CS solution. The stress σ_{xx} obtained using PIM-CS is continuous in the entire problem domain

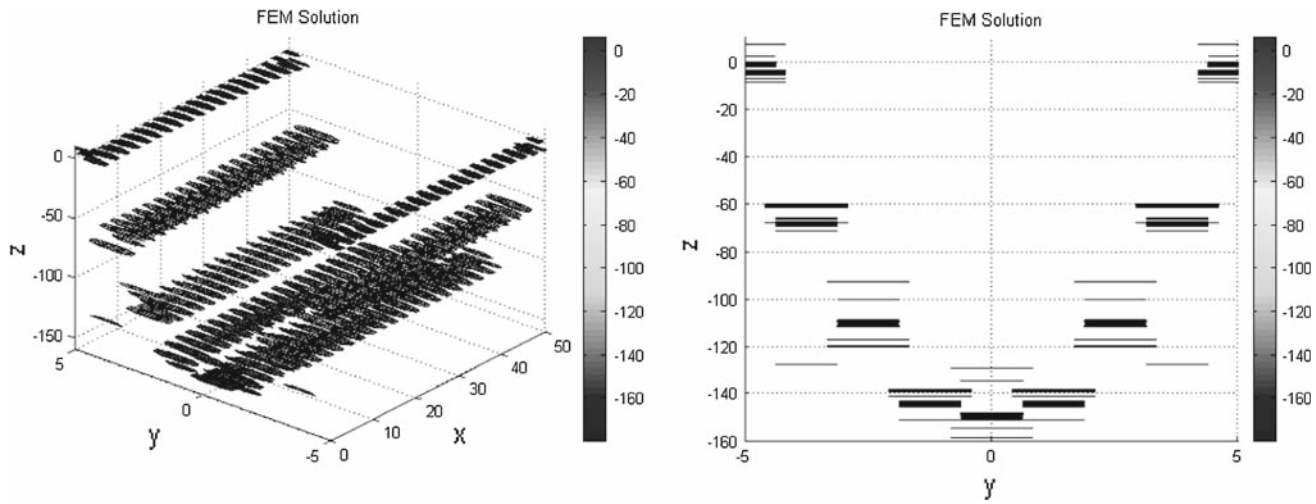

Fig. 12 Stress σ_{xy} distribution of the FEM solution. It is discontinuous and has jumps

7.6 Crack problem: a plate with an edge crack

A plate with an edge crack is now studied, whose geometry is shown in Fig. 30. The exact stress solution of stress near the crack tip is given in [62]. The computed strain energy and convergence in energy norm for different α are plotted in Figs. 31 and 32, respectively. It is found again that the linear PIM-CS produces superconvergent solutions in energy norm: convergence rate is 1.64 when $\alpha = 1$ and 1.98 when $\alpha = 1.06$. When x-Galerkin weak form ($\alpha = 1$) is used, the accuracy of the linear PIM-CS solution is very high in energy norm. It is about 10 times more accurate than that of the linear FEM using the same mesh.

7.7 PIM-CS with high order polynomials interpolation

We now examine the 2D cantilever beam using quadratic PIM-CS that uses quadratic polynomial interpolation for displacement field. In this case, we need to choose 6 nodes for the interpolation for the point of interest based on the same triangular cells. This can be done easily by simply choose the three vertices of the triangle hosting the point of interest, and the three vertices of the three neighboring triangles sharing the edges with the hosing triangle that are opposite to the shared edges. The details of construction of quadratic PIM shape function based on triangular cells can be found in [40].

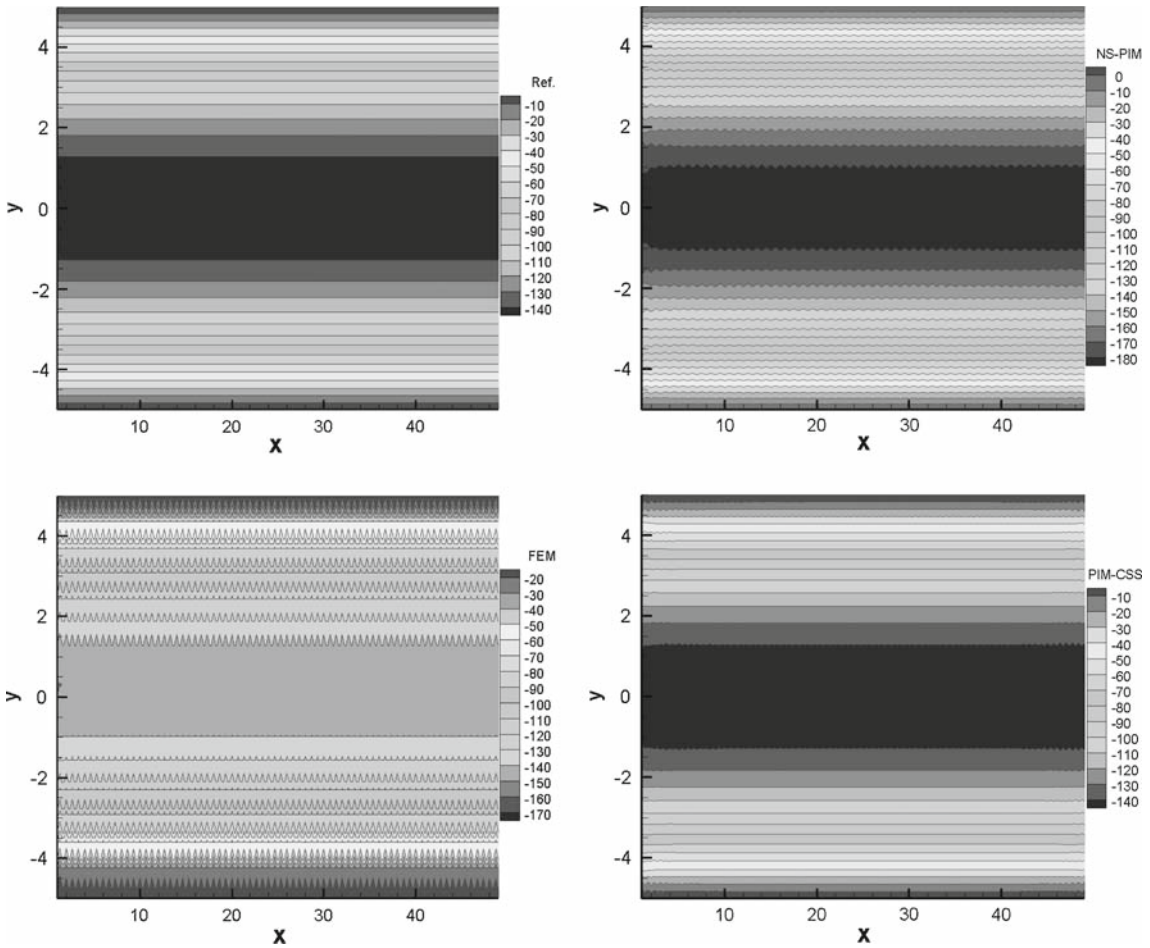

Fig. 13 Contour plots of stress σ_{xy} obtained using different numerical methods. The PIM-CS solution is very close to the exact solution

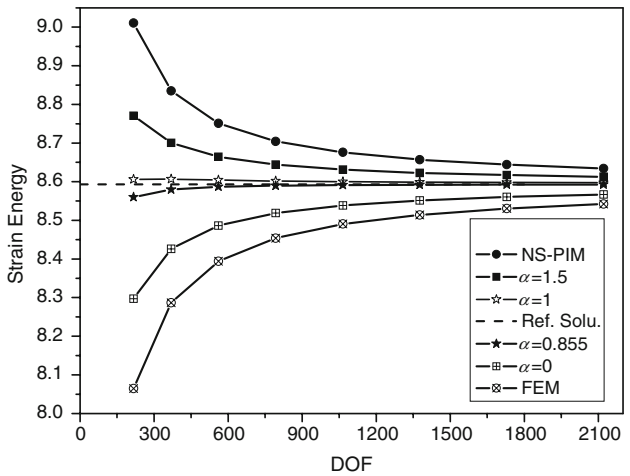

Fig. 14 Upper and lower bound solutions of the PIM-CS for 2D beam. When $\alpha = 1$, the x-Galerkin weak form is used

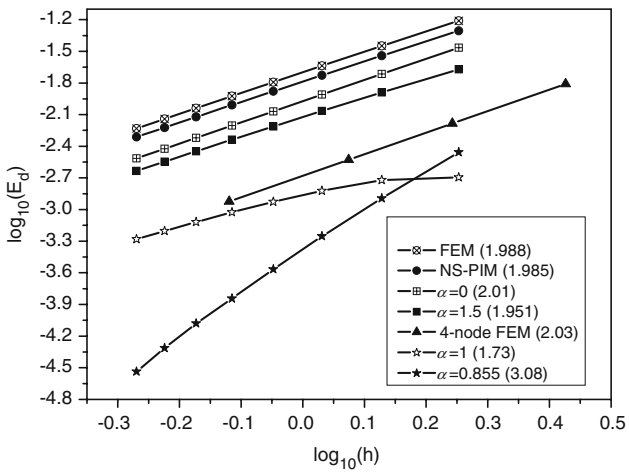

Fig. 15 Convergence of the PIM-CS solution in displacement norm for different α. The x-Galerkin weak form is used when $\alpha = 1$. Super-convergence is observed when $\alpha = 0.855$

To study the convergence of the quadratic PIM-CS solution, the strain energy is computed using different α and the results are plotted in Fig. 33. It is found that the solution of quadratic PIM-CS is more accurate than that of linear PIM-CS. The quadratic PIM-CS produces also upper bound solutions of the exact solution when $\alpha = 1.25$, and lower bound

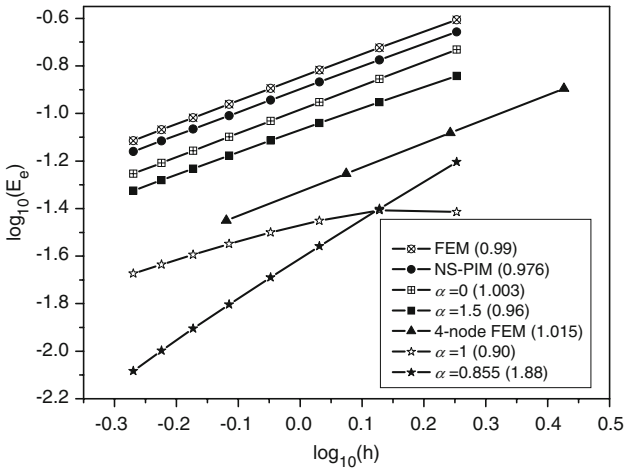

Fig. 16 Convergence of the PIM-CS solution in energy norm for different α. The x-Galerkin weak form is used when $\alpha = 1$. Superconvergence is observed when $\alpha = 0.855$

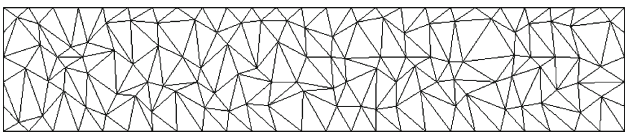

Fig. 17 Illustration of irregular mesh used to examine how the regularity of the point distribution influences the quality of the results

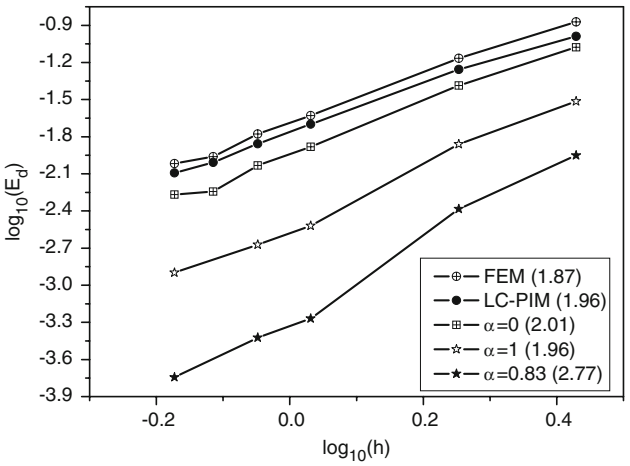

Fig. 18 Convergence of the PIM-CS solution in displacement norm using the irregular mesh. Superconvergence is still observed when $\alpha = 0.83$, and very high accurate solution can be obtained when the x-Galerkin weak form ($\alpha = 1$) is used

solutions when $\alpha = 0.5$. Using Eqs. (77) and (78), errors in displacement and energy norms are calculated and plotted against the average nodal spacing (h) in Figs. 34 and 35. From these figures, it is seen that when $\alpha = 0.5$ and $\alpha = 0.71$, the accuracy and convergence rates in both displacement norm and energy norm are very high, which shows that the quadratic PIM-CS is of superconvergence.

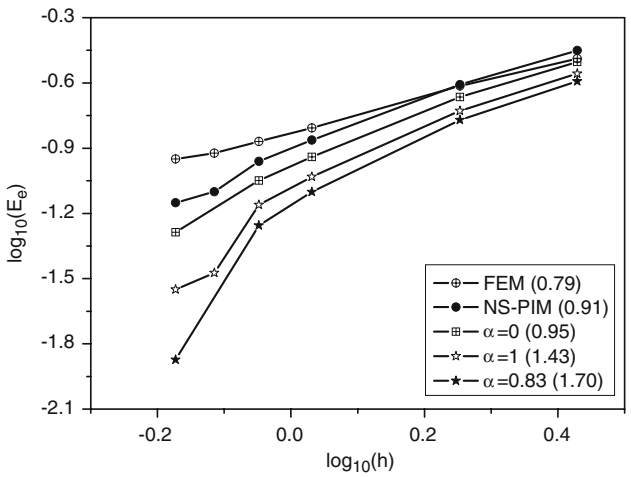

Fig. 19 Convergence of the PIM-CS solution in energy norm using the irregular mesh. Superconvergence is observed when $\alpha = 0.83$, and very accurate solution can also be obtained using the x-Galerkin weak form ($\alpha = 1$)

7.8 Discussions and comparisons on FEM, NS-PIM and PIM-CS

We present a comparison discussion for FEM, NS-PIM and PIM_CS models.

Remark 2 The strain field of the PIM-CS is a linear interpolation of locally smoothed strain at points. Not only the averaged strain but also the local variation effects of the strain field are taken into account in the PIM-CS. The PIM-CS model using exactly the same triangular mesh can behave "softer" than FEM and "stiffer" than NS-PIM; both accuracy and convergence rate are much higher than those of FEM and NS-PIM; furthermore the stress is continuous in the entire problem domain.

Remark 3 It is clear from Sect. 4 that not only displacement field but also strain field can be constructed using the point interpolation method. This is the first time to use the point interpolation method for strain field construction in meshfree methods. This similar was done in the $a-$FEM [32].

Remark 4 The stiffness matrix obtained using PIM-CS is symmetric with the same dimensions as that of FEM when the same mesh is used.

Remark 5 Both the FEM based on the standard Galerkin weak form and the NS-PIM based on the generalized smoothed Galerkin weak form [30] are variationally consistent, if the solution is sought in a Hilbert space. However, PIM-CS is in general not vairationally consistent, even if the solution is sought in a Hilbert space. This shows an important fact that variational consistence is not a necessary condition to

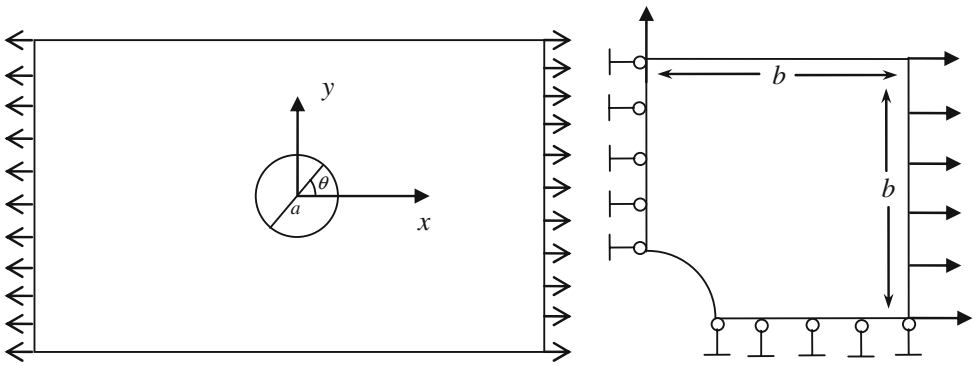

Fig. 20 Infinite 2D solid with a hole subjected to a tensile force and its quarter model

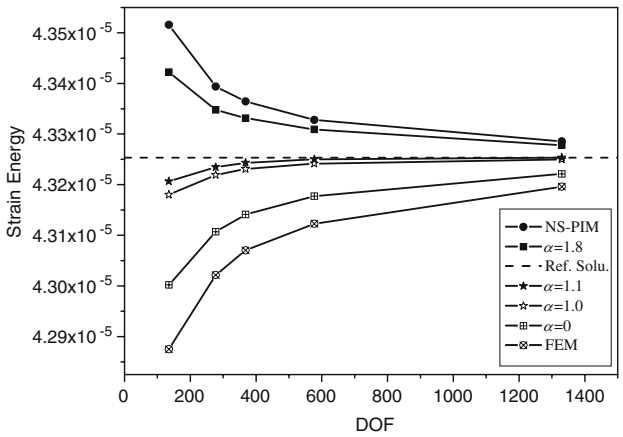

Fig. 21 Lower and upper bound solutions of the PIM-CS for 2D solid with hole. When $\alpha = 1$, the x-Galerkin weak form is used

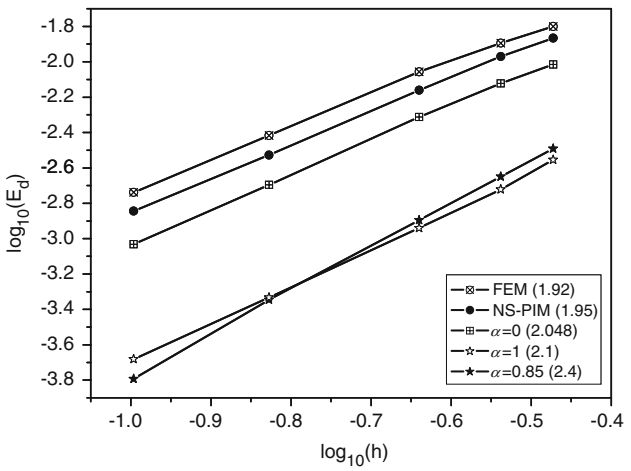

Fig. 22 Convergence of the PIM-CS in displacement norm for 2D solid with hole. The x-Galerkin weak form is used when $\alpha = 1$. Superconvergence is observed when $\alpha = 0.85$

derive a numerical method. Many numerical results [32,49] and the numerical results obtained in this paper show that a variationally inconsistent model can work very effectively, and can have unique properties.

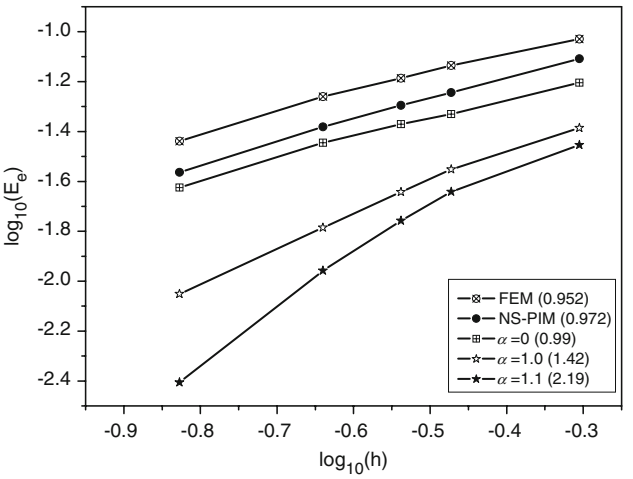

Fig. 23 Convergence of the PIM-CS in energy norm for 2 D sold with hole. The x-Galerkin weak form is used when $\alpha = 1$. Superconvergence is observed when $\alpha = 1.0$ and 1.1

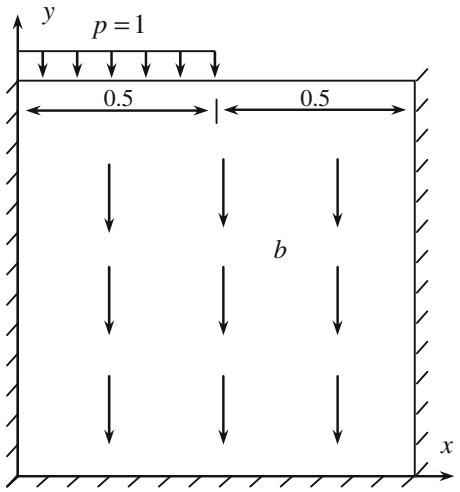

Fig. 24 A square solid with body force subjected to a uniform pressure

Remark 6 PIM-CS is equipped with a real adjustable parameter α, and hence can bound the solutions from the both sides of the exact solution. Therefore, PIM-CS is capable of

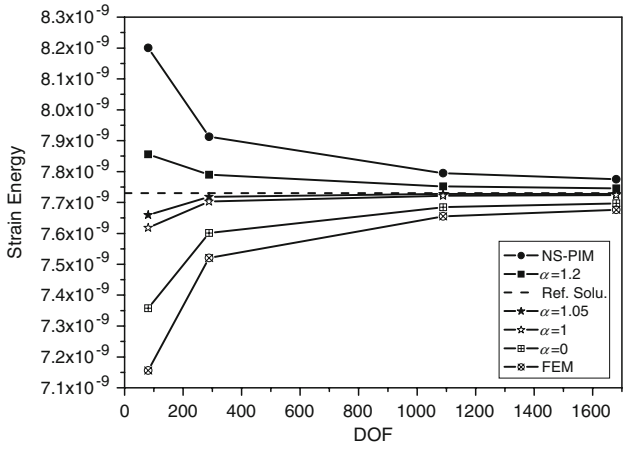

Fig. 25 Upper and lower bound solution of the PIM-CS for different α. When $\alpha = 1$, the x-Galerkin weak form is used

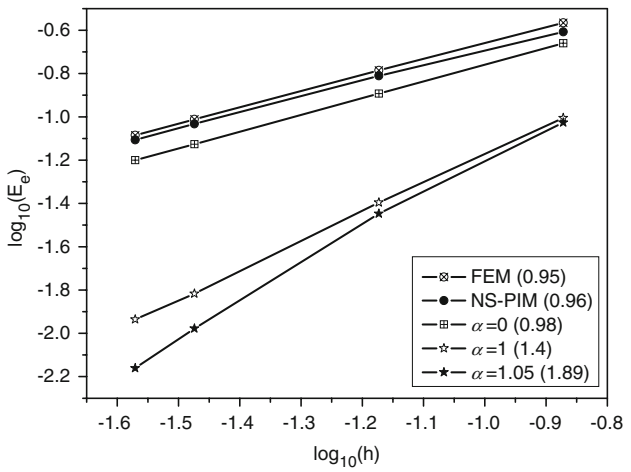

Fig. 26 Convergence of the PIM-CS in energy norm for different α. The x-Galerkin weak form is used when $\alpha = 1$. Superconvergence is observed when $\alpha = 1.0$ and $\alpha = 1.05$

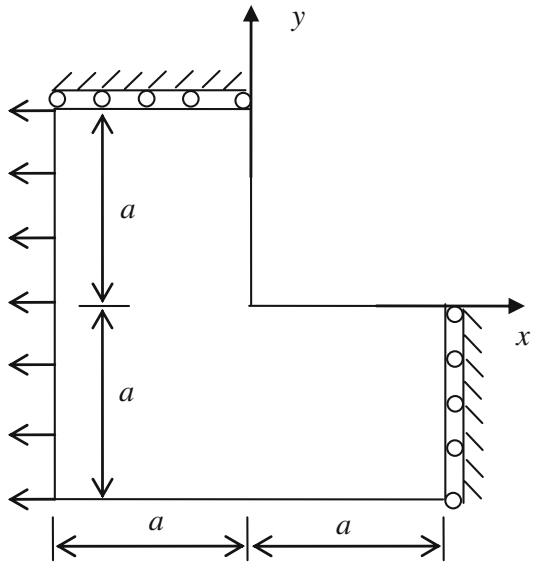

Fig. 27 L-shaped plate subjected to uniform tensile stress

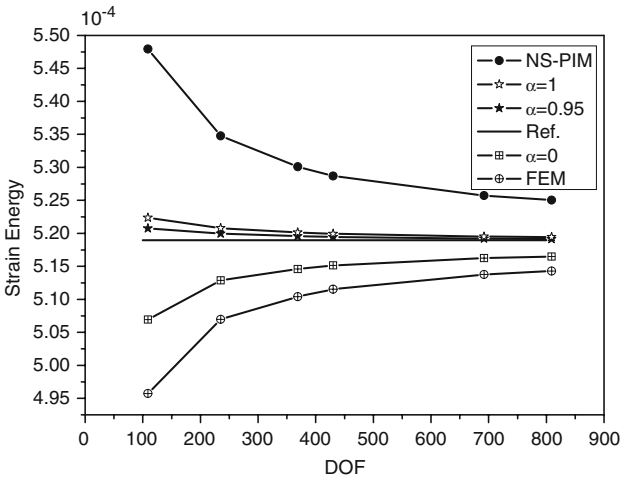

Fig. 28 Upper and lower bound solution in energy norm of PIM-CS used in the L-shaped component problem. When $\alpha = 1$, the x-Galerkin weak form is used

obtaining the exact solution using a finite number of triangular meshes.

Remark 7 The numerical results show that PIM-CS is of superconvergence for a properly selected α. However, α is in general problem-dependent and it needs taking a number of trials to find a good α for a practical problem.

Remark 8 When $\alpha = 1$, the PIM-CS becomes a x-Galerkin model. From all these numerical examples it is clearly seen that in an x-Galerkin model, the accuracy and the convergence rate are very high in both displacement and energy norms. It is about 10 times more accurate than that of standard Galerkin mode (FEM) using the same mesh. Therefore, for avoiding the difficulty to find the "good" α, we can simply use the x-Galerkin weak form ($\alpha = 1$) to obtain ultra accurate solutions.

8 Conclusions

In this work, a point interpolation method with continuous strain field is developed using the PIM shape functions for constructing both the displacement and the strain fields. A general parameterized mixed functional is proposed for establishing models with superconvergent solutions. We proved theoretically (1) when the same mesh is used, the strain energy obtained from the PIM-CS is in between those from the compatible FEM and the NS-PIM models; (2) the exact solution is bounded by those of PIM-CS with $\alpha = \alpha_1 \in [\frac{3}{2}, \frac{5}{2}]$ from above and $\alpha = \alpha_0 \in [-\frac{3}{2}, -\frac{1}{2}]$ from below; (3) There is an α at which the PIM-CS give the exact solution

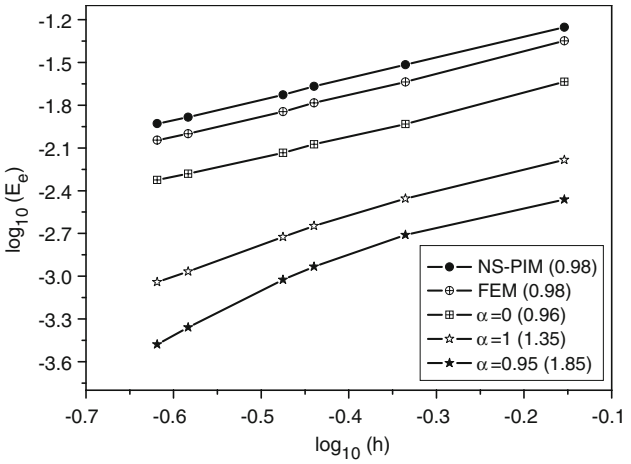

Fig. 29 Convergence of PIM-CS solution in energy norm for different α used in the L-shaped component problem. Superconvergence is observed when $\alpha = 0.95$, and the x-Galerkin weak form ($\alpha = 1$) produces solution of very high accuracy (about 10 times more accurate than that of FEM) and superconvergence

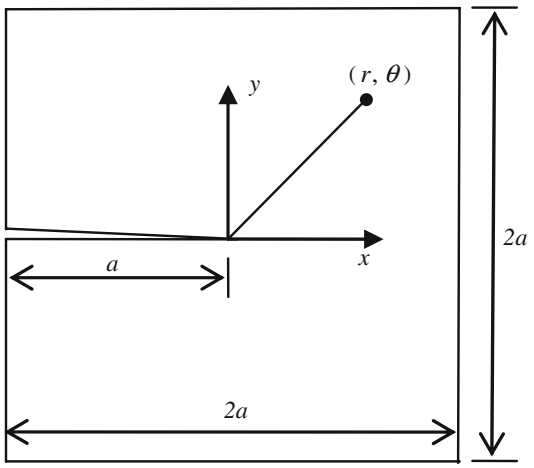

Fig. 30 Geometry of a cracked plate

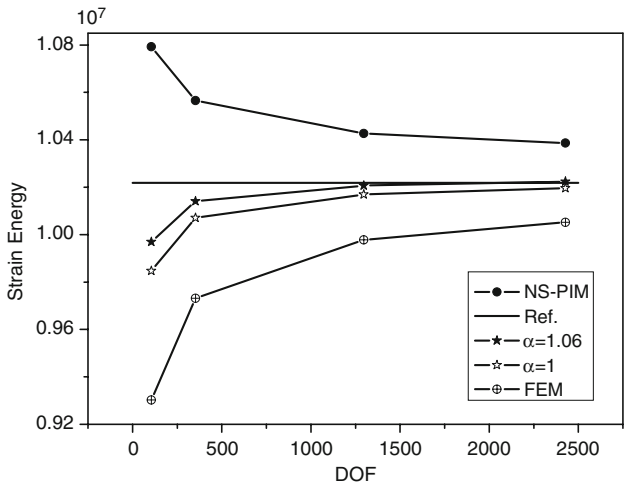

Fig. 31 Upper and lower bound solution in energy norm of PIM-CS for different α used in the crack problem. When $\alpha = 1$ the x-Galerkin weak form is used

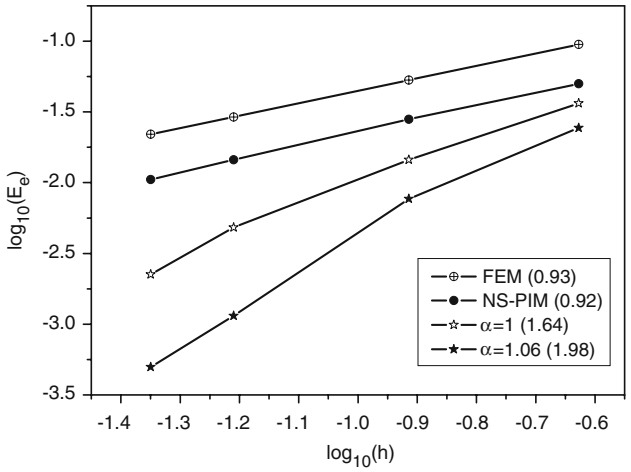

Fig. 32 Convergence of PIM-CS solution in energy norm for different α used in the crack problem. Superconvergence is observed when $\alpha = 1.0$ and $\alpha = 1.06$, and the x-Galerkin weak form ($\alpha = 1$) produces solution of very high accuracy (about 10 times more accurate than that of FEM) and superconvergence

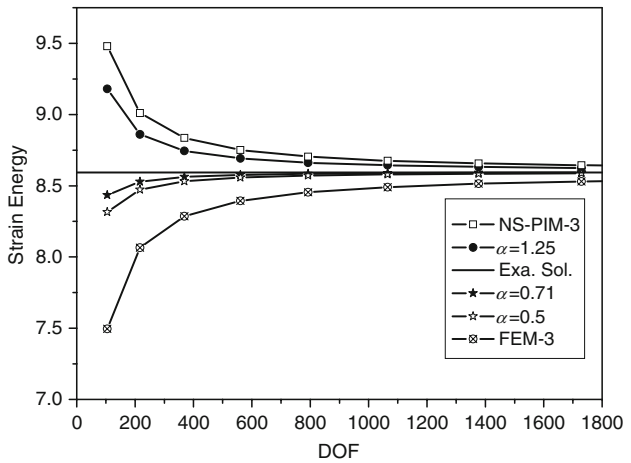

Fig. 33 Upper and lower bounds solution of strain energy for different α used in PIM-CS with quadratic interpolation, in comparison with the solutions of linear interpolation using 3-node background cells (NS-PIM-3 and FEM-3)

in energy norm; (4) the x-Galerkin weak form is not variationally consistent, but proven to be stable and convergent to the exact solution.

Intensive numerical studies have verified the theorems, convergence, bounds property of strain energy, continuity of strain, and superconvergence of the PIM-CS:

(1) The PIM-CS is convergent for any $\alpha \in [\alpha_0, \alpha_1]$ with continuous strain/stress field in the entire domain.
(2) PIM-CS uses triangular background cells can produce even more accurate solution than the quadrilateral elements of FEM;

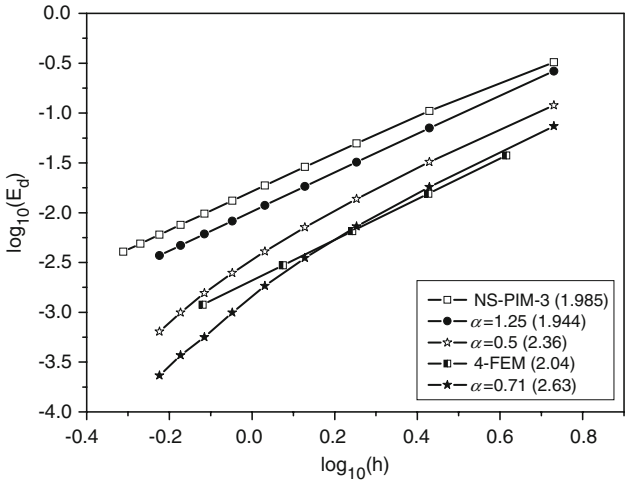

Fig. 34 Convergence of PIM-CS solution in displacement norm for different α used in PIM-CS with quadratic interpolation

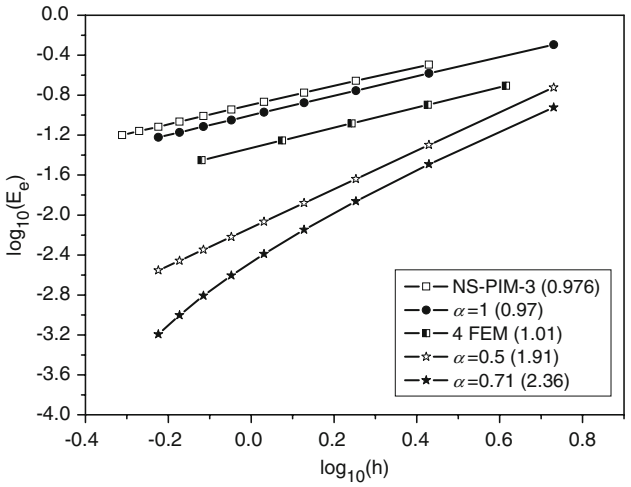

Fig. 35 Convergence of PIM-CS solution in energy norm for different α used in PIM-CS with quadratic interpolation

(3) For a properly chosen α, PIM-CS can produce upper bound, lower bound and superconvergent solutions, as desired.

(4) The new x-Galerkin weak form ($\alpha = 1$) produces solutions of very high accuracy, which is about one order more accurate than that of the FEM solution using the same linear triangular elements.

Acknowledgments This work was supported in part by the National Natural Science Foundation of China under Grants 10532050, 10501017, 60673023, and by the 985 program of Jilin University, China. The authors also thank to the support of Centre for ACES and Singapore-MIT Alliance (SMA), National University of Singapore.

References

1. Zienkiewicz OC, Taylor RL (2000) The fnite element method, 5th edn. Butterworth Heinemann, Oxford
2. Liu GR, Quek SS (2003) The finite element method: a practical course. Butterworth Heinemann, Oxford
3. Brenner SC, Scott LR (1994) The mathematical theory of finite element methods. Springer, New York
4. Dietrich Braess (2007) Finite elements: theory, fast solvers, and applications in solid mechanics. Cambridge University Press, London
5. Samarskiĭ AA, Vabishchevich PN, Vulkov LG (1999) Finite difference methods: theory and applications. Nova Science Publishers, New York
6. Forsythe GE, Wasow WR (1960) Finite-difference methods for partial differential equations. Cambridge University Press, New York
7. LeVeque RJ (2002) Finite volume methods for hyperbolic problems. Cambridge University Press, New York
8. Li RH, Chen ZY, Wu W (2000) Generalized difference methods for differential equations: numerical analysis of finite volume methods. Marcel Dekker, New York
9. Lucy LB (1977) A numerical approach to testing the fission hypothesis. Astron J 8:1013–1024
10. Liu GR, Liu MB (2003) Smoothed particle hydrodynamics—a meshfree practical method. World Scientific, Singapore
11. Nayroles B, Touzot G, Villon P (1992) Generalizing the finite element method: diffuse approximation and diffuse elements. Computat Mech 10:307–318
12. Belytschko Y, Lu YY, Gu L (1994) Element-free Galerkin methods. Int J Numer Methods Eng 37:229–256
13. Liu WK, Jun S, Zhang YF (1995) Reproducing kernel particle methods. Int J Numer Methods Eng 20:1081–1106
14. Atluri SN, Zhu T (1998) A new meshless local Petrov–Galerkin (MLPG) approach in computational mechanics. Computat Mech 22:117–127
15. Liu GR, Gu YT (2001) A point interpolation method for two-dimensional solids. Int J Numer Methods Eng 50:937–951
16. Wang JG, Liu GR (2002) A point interpolation meshless method based on radial basis functions. Int J Numer Methods Eng 54:1623–1648
17. Liu GR (2002) Meshfree methods: moving beyond the finite element method. CRC Press, Boca Raton
18. Liu GR, Gu YT (2005) An introduction to meshfree methods and their programming. Springer, Dordrecht
19. Onate E, Idelsohn S, Zienkiewicz OC, Taylor RL (1996) A finite point method in computational mechanics. Applications to convective transport and fluid flow. Int J Numer Methods Eng 39(22):3839–3866
20. Onate E, Idelsohn S, Zienkiewicz OC, Taylor RL, Sacco C (1996) A stabilized finite point method for analysis of fluid mechanics problems. Comput Methods Appl Mech Eng 139(1–4):315–346
21. Rabczuk T, Belytschko T, Xiao SP (2004) Stable particle methods based on Lagrangian kernels. Comput Methods Appl Mech Eng 193(12–14):1035–1063
22. Swegle LW, Hichks DL, Hicks , Attaway SW (1995) Smooth particle hydrodynamics stability analysis. J Computat Phys 116:123–134
23. Xiao SP, Belytschko T (2005) Material stability analysis of particle methods. Adv Computat Math 23:171–190
24. Dyka CT (1994) Addressing tension instability in SPH methods. NRL/MR/6384, NRL
25. Rabczuk T, Bordas S, Zi GS (2007) A three-dimensional meshfree method for continuous crack initiation, nucleation and propagation. Stat Dyn 40(3):473–495
26. Bordas X, Rabczuk T, Zi G (2007) Three-dimensional crack initiation, propagation, branching and junction in non-linear materials by an extended meshfree method without asymptotic enrichment. Eng Fract Mech. doi:10.1016/j.engfracmech.2007.05.010

27. Nguyen VP, Rabczuk T, Bordas S, Duflot M (2008) Meshfree methods: review and key computer implementation aspects. Mathematics and Computers in Simulation. doi:10.1016/j.matcom.2008.01.003
28. Nguyen VP, Rabczuk T, Bordas S, Duflot M (2008) Meshless methods: a review and computer implementation aspects. Math Comput Simul (in press)
29. Liu GR (2008) A generalized gradient smoothing technique and the smoothed bilinear form for Galerkin formulation of a wide class of computational methods. Int J Computat Methods 5(2):199–236
30. Liu GR, Zhang GY (2008) Upper bound solution to elasticity problems: A unique property of the linearly conforming point interpolation method (LC-PIM). Int J Numer Methods Eng 74:1128–1161
31. Pian THH, Wu CC (2006) Hybrid and incompatible finite element methods. CRC Press, Boca Raton
32. Liu GR, Nguyen-Thoi T, Lam KY (2008) A novel alpha finite element method (αFEM) for exact solution to mechanics problems using triangular and tetrahedral elements. Comput Methods Appl Mech Eng (in press). doi:10.1016/j.cma.2008.03.011
33. Liu GR, Dai KY, Nguyen-Thoi T (2007) A smoothed element method for mechanics problems. Computat Mech 39:859–877
34. Liu GR, Nguyen-Thoi T, Dai KY, Lam KY (2007) Theoretical aspects of the smoothed finite element method (SFEM). Int J Numer Methods Eng 71:902–930
35. Dai KY, Liu GR, Nguyen-Thoi T (2007) An n-sided polygonal smoothed finite element method (nSFEM) for solid mechanics. Finite Elem Anal Des 43:847–860
36. Nguyen-Thoi T, Liu GR, Dai KY, Lam KY (2007) Selective smoothed finite element method. Tsinghua Sci Technol 12(5):497–508
37. Dai KY, Liu GR (2007) Free and forced vibration analysis using the smoothed finite element method (SFEM). J Sound Vib 301:803–820
38. Cui XY, Liu GR, Li GY, Zhao X, Nguyen-Thoi T, Sun GY (2008) A smoothed finite element method (SFEM) for linear and geometrically nonlinear analysis of plates and shells. Comput model Eng Sci 28:109–125
39. Liu GR, Nguyen-Thoi T, Nguyen XH, Lam KY (2007) A node-based smoothed finite element method (N-SFEM) for upper bound solutions to solid mechanics problems. Comput Struct (revised)
40. Liu GR, Zhang GY, Dai KY, Wang YY, Zhong ZH, Li GY, Han X (2005) A linearly conforming point interpolation method (LC-PIM) for 2D solid mechanics problems. Int J Computat Methods 2:645–665
41. Liu GR, Nguyen-Thoi T, Nguyen XH, Lam KY (2007) An edge-based smoothed finite element method (E-SFEM) for static, free and forced vibration analysis. J Sound Vib (revised)
42. Nguyen-Xuan H and Bordas S and Nguyen-Dang H, (2007) Smooth finite elements: convergence, accuracy and properties. Int J Numer Methods Eng (in press). doi:10.1002/nme.2146
43. Nguyen-Xuan H, Rabczuk T, Bordas S, Debongnie JF (2008) A smoothed finite element method for plate analysis. Comput Methods Appl Mech Eng 197(13–16):1184–1203
44. Nguyen-Thanh N, Timon Rabczuk, Nguyen-Xuan H, Stéphane PA Bordas (2008) A smoothed finite element method for shell analysis. Comput Methods Appl Mech Eng (in press)
45. Chen JS, Wu CT, Yoon S, You Y (2001) A stabilized conforming nodal integration for Galerkin mesh-free methods. Int J Numer Methods Eng 50:435–466
46. Zhang GY, Liu GR, Wang YY, Huang HT, Zhong ZH, Li GY, Han X (2007) A linearly conforming point interpolation method (LC-PIM) for three-dimensional elasticity problems. Int J Numer Methods Eng 72:1524–1543
47. Li Y, Liu GR, Luan MT, Dai KY, Zhong ZH, Li Gy, Han X (2007) Contact analysis for solids based on linearly conforming radial point interpolation method. Computat Mech 39:859–877
48. Liu GR, Li Y, Dai KY, Luan MY, Xue W (2006) A linearly conforming RPIM for 2D solid mechanics. Int J Computat Methods 3:401–428
49. Liu GR, Xu X, Zhang GY, Nguyen-Thoi T (2008) A superconvergent point interpolation method (SC-PIM) with piecewise linear strain field using triangular mesh. Int J Numer Methods Eng (in press)
50. Wu, SC, Zhang HO, Liu GR, Zhang GY (2008) A node-based smoothed point interpolation method (NS-PIM) for thermo-elastic problems with solution bounds. Int J Heat Mass Transf (in press)
51. Wu SC, Liu GR, Zhang HO, Zhang GY (2008) A node-based smoothed point interpolation method (NS-PIM) for three-dimensional thermo-elastic problems. Numer Heat Transf Part A Appl (accepted)
52. Liu GR, Zaw K, Wang YY (2008) Rapid inverse parameter estimation using reduced-basis approximation with asymptotic error estimation. Comput Methods Appl Mech Eng. doi:10.1016/j.cma.2008.03.012
53. Liu GR, Zaw K, Wang YY, Deng B (2008) A novel reduced-basis method with upper and lower bounds for real-time computation of linear elasticity problems. Comput Methods Appl Mech Eng (in press)
54. Jindrich N, Ivan H (1981) Mathematical theory of elastic and elasto-plastic bodies: an introduction. Elsevier, New York
55. Liu GR (2008) A weakened weak (W2) form for unified formulation of compatible and incompatible displacement methods of excellent properties. Int J Numer Methods Eng (submitted)
56. Liu GR, Xu XG (2007) An adaptive gradient smoothing method (GSM) for fluid dynamics problems (accepted)
57. Liu GR, Zhang J, Lam KY (2008) A gradient smoothing method (GSM) with directional correction for solid mechanics problems. Computat Mech 41:457–472
58. Wu HC (1982) Variational principle in elasticity and applications. Scientific Press, Beijing
59. Stroud AH, Secrest Don (1966) Gaussian quadrature formulas. Prentice-Hall, Englewood Cliffs
60. Li RH, Chen ZY (1994) Generalized difference methods for differential equations. Jilin University Press, Changchun
61. Timoshenko SP, Goodier JN (1970) Theory of elasticity, 3rd edn. McGraw, New York
62. Anderson TL (1991) Fracture mechanics: fundamentals and applications, 1st edn. CRC Press, Boca Raton